

Pickup Ions at Dione and Enceladus

*E. Sittler, R.E. Johnson, S. Jurac, J. Richardson,
M. McGrath, F. Crary, D. Young, and J.E. Nordholt*

The NASA STI Program Office ... in Profile

Since its founding, NASA has been dedicated to the advancement of aeronautics and space science. The NASA Scientific and Technical Information (STI) Program Office plays a key part in helping NASA maintain this important role.

The NASA STI Program Office is operated by Langley Research Center, the lead center for NASA's scientific and technical information. The NASA STI Program Office provides access to the NASA STI Database, the largest collection of aeronautical and space science STI in the world. The Program Office is also NASA's institutional mechanism for disseminating the results of its research and development activities. These results are published by NASA in the NASA STI Report Series, which includes the following report types:

- **TECHNICAL PUBLICATION.** Reports of completed research or a major significant phase of research that present the results of NASA programs and include extensive data or theoretical analysis. Includes compilations of significant scientific and technical data and information deemed to be of continuing reference value. NASA's counterpart of peer-reviewed formal professional papers but has less stringent limitations on manuscript length and extent of graphic presentations.
- **TECHNICAL MEMORANDUM.** Scientific and technical findings that are preliminary or of specialized interest, e.g., quick release reports, working papers, and bibliographies that contain minimal annotation. Does not contain extensive analysis.
- **CONTRACTOR REPORT.** Scientific and technical findings by NASA-sponsored contractors and grantees.

- **CONFERENCE PUBLICATION.** Collected papers from scientific and technical conferences, symposia, seminars, or other meetings sponsored or cosponsored by NASA.
- **SPECIAL PUBLICATION.** Scientific, technical, or historical information from NASA programs, projects, and mission, often concerned with subjects having substantial public interest.
- **TECHNICAL TRANSLATION.** English-language translations of foreign scientific and technical material pertinent to NASA's mission.

Specialized services that complement the STI Program Office's diverse offerings include creating custom thesauri, building customized databases, organizing and publishing research results . . . even providing videos.

For more information about the NASA STI Program Office, see the following:

- Access the NASA STI Program Home Page at <http://www.sti.nasa.gov/STI-homepage.html>
- E-mail your question via the Internet to help@sti.nasa.gov
- Fax your question to the NASA Access Help Desk at (301) 621-0134
- Telephone the NASA Access Help Desk at (301) 621-0390
- Write to:
NASA Access Help Desk
NASA Center for AeroSpace Information
7121 Standard Drive
Hanover, MD 21076-1320



Pickup Ions at Dione and Enceladus

E. Sittler
Goddard Space Flight Center, Greenbelt, MD

R.E. Johnson
University of Virginia, Charlottesville, VA

S. Jurac, J. Richardson
Massachusetts Institute of Technology, Cambridge, MA

M. McGrath
Space Telescope Institute, Baltimore, MD

F. Crary, D. Young
University of Michigan, Ann Arbor, MI

J.E. Nordholt
Los Alamos National Laboratory, NM

National Aeronautics and
Space Administration

Goddard Space Flight Center
Greenbelt, Maryland 20771

Available from:

NASA Center for AeroSpace Information
7121 Standard Drive
Hanover, MD 21076-1320
Price Code: A17

National Technical Information Service
5285 Port Royal Road
Springfield, VA 22161
Price Code: A10

Pickup Ions at Dione and Enceladus

by Ed Sittler¹, R. E. Johnson², S. Jurac³, J. Richardson³,

M. McGrath⁴, F. Crary⁵, D. Young⁵ and J.E. Nordholt⁶

¹NASA/Goddard Space Flight Center

²University of Virginia, Charlottesville, VA

³Massachusetts Institute of Technology, Cambridge, MA

⁴Space Telescope Science Institute, Baltimore, MD

⁵University of Michigan, Ann Arbor, MI

⁶Los Alamos National Laboratory, NM

Abstract

Voyager images of the icy satellites of Saturn, Dione and Enceladus, suggest they have been geologically active and are not only composed of ice. Recent observations by HST have shown the presence of ozone at both Dione and Rhea which also implies the presence of molecular oxygen at these bodies. The Cassini Plasma Spectrometer (CAPS) will provide the capability to determine the global composition of these bodies by measuring the pickup ions produced by the ionization of their sputter produced atmospheres. We will present a model of these atmospheres and associated pickup ions and demonstrate CAPS ability to distinguish the freshly produced picked up ions from the ambient plasma. Such ions are expected to form a ring distribution that will have a uniquely different energy-angle dependence than the ambient plasma ions. In the case of Dione we expect the potential for a moderate strength interaction for which both Voyager 1 and Pioneer 11 spacecraft measured ion cyclotron waves centered on the Dione L shell and near the equatorial plane. Since Enceladus may be the source of the E-ring, some surprises may be encountered during its close encounter with the Cassini spacecraft. In the case of Dione we will show that a wake pass at 500 km altitude is more than an order of magnitude better than an upstream pass at 500 km altitude. Pickup ion detection for minor ion species such as NH_3^+ is possible for 500 km altitude wake pass but not for a 500 km altitude upstream pass at closest approach. For navigation reasons a 100 km pass is not allowed and therefore it is essential to have a wake pass to maximize the science return for a targeted flyby with Dione. The CAPS observations when combined with magnetometer, plasma wave and energetic particle observations will allow us to estimate the source of ions into Saturn's magnetosphere due to these two bodies and to characterize the nature of the interaction with Saturn's magnetosphere.

Contents

1. Introduction	1
2. CAPS Instrument Description and Capabilities with Respect to Targeted Icy Satellite Encounters	4
3. Model of Sputtered Atmospheres for Dione and Enceladus	5
4. Estimates of Pickup Ion Densities as a function of Height for Dione and Enceladus	7
4.1 Wake Pass	7
4.2 Upstream Passes	15
5. Ring Distribution Simulations.	20
6. Simulated E/Q Versus TOF Spectrograms	25
7. Summary and Conclusion	37
8. References	39

1. Introduction

In this paper we will be primarily concerned with the interaction of Saturn's magnetosphere with its icy satellites Dione and Enceladus. In the future we plan to also look at the other icy satellites Mimas, Tethys and Rhea; in the case of Rhea finite gyro-radii effects will be important. The icy satellite interaction with Saturn's magnetosphere can provide very important information about the bulk properties and surface properties of these bodies by detecting the pickup ions produced by the ionization of their sputtered neutral atmosphere (see Johnson and Sittler, 1990). The icy satellites are believed to be composed primarily of ice with trace amounts of O_2 , O_3 and other possible frozen volatiles such as CH_4 , NH_3 , CO_2 , and possible dark components such as C and S (see Morrison et al., 1984).

At present, most of our knowledge of the Saturnian system can be traced to the pioneering observations of Saturn's plasma population, energetic particle population, magnetic fields, plasma waves and remote sensing observations from the Pioneer 11 and Voyager 1 and 2 encounters. The papers by Frank et al. (1980), Lazarus and McNutt (1983), Sittler et al. (1983), and Richardson (1986) summarize the first observations of Saturn's plasma environment. The energetic particle populations of Saturn's magnetosphere were summarized in papers by Fillius and McIlwain (1980), Van Allen (1980), Fillius et al. (1980), Vogt et al. (1982), Krimigis and Armstrong (1982), Schardt and McDonald (1983), Krimigis et al. (1983), and Van Allen (1984). More recently, Maurice et al. (1996), Paranicos et al. (1997) and Jurac et al. (2001) have reanalyzed the Voyager plasma and energetic particle data to put it in a more synergistic form. Richardson and Sittler (1990) combined the Voyager ion and electron plasma observations to construct an empirical model of Saturn's plasma environment inside of about $15 R_S$. In concert Johnson et al. (1989) constructed from all these observations a model of a neutral cloud torus that surrounds Saturn and is primarily due

to sputtered neutrals coming from the icy satellites of Saturn. Richardson et al. (1986) made the first attempt at combining all these various data sets to construct a semi-empirical model of Saturn's plasma and neutral environment including various collisional and ionization processes and radial diffusion which enforced constraints on the plasma source strength and the rate of radial diffusion.

This work was followed by the discovery by using HST of a relatively large toroidal cloud of OH that was surrounding Saturn with densities as high as 500 cm^{-3} near the L shell of Enceladus (Shemansky et al., 1993; Hall et al. 1996; and Richardson et al. 1998). This discovery put into question the original work by Johnson et al. (1989) for which it was believed that the icy satellites dominated the neutral environment around Saturn. In order to reconcile these new observations Richardson et al. (1998) invoked rapid radial transport with time scales at $6 R_S$ of only 5 days while in the original work by Richardson et al. (1986) it was 700 days. Results by Shi et al. (1995) and Jurac et al. (2001) now show that the icy satellites and the observed grains in the E ring each contribute less than 10% of the observed neutral population. The detection of ozone, O_3 , in the surface ice of Rhea and Dione (Noll et al. (1997)) for which the column densities were $\sim 2 \times 10^{16} \text{ mol/cm}^2$ meant that column densities of O_2 could be as high a 10^{19} mol/cm^2 within the icy mantles of these bodies. Since the temperature of these bodies are $\sim 75^\circ\text{K}$ to 100°K (Hanel et al., 1981, 1982), there could exist a significant gravitationally bound O_2 , O_3 (i.e., since ozone is unstable it might not contribute to an atmosphere around these bodies) atmosphere at Dione and Enceladus with the scale heights for O_2 of 117 km and 227 km, respectively. If the O_2 , believed to be trapped in the icy surfaces of these bodies, contribute to these atmospheres then the peak neutral densities could be as high as $8.3 \times 10^{11} \text{ mol/cm}^3$ for Dione and $4.3 \times 10^{11} \text{ mol/cm}^3$ for Enceladus. Therefore, a wake pass of Dione may see large quantities of pickup O_2^+ and O_3^+ near the limb of Dione; while an up-

stream pass at 500 km altitude would probably not detect such an atmosphere. In the case of Enceladus the atmosphere would be less bound with a significant fraction of the O_2 and O_3 on escape trajectories. We may also expect significant amounts of CO_2 to be present, since CO_2 was detected at the Galilean moons (McCord et al., 1998) and in the atmosphere of Titan (Samuelson et al., 1983) where CO was also detected (Lutz et al., 1983). The planned close encounters by Cassini of these bodies will allow us to develop a more accurate picture of their role in neutral cloud production and, thus, in the plasma and energetic particle production within Saturn's magnetosphere.

Since these bodies are deep within the magnetosphere of Saturn and its radiation belts, they are expected to have, at minimum, a tenuous atmosphere due to sputtering induced by energetic particle bombardment and bombardment by the ambient plasma. The icy satellites should also be exposed to micrometeorite bombardment which will produce a porous regolith on their surface and the emission of particulates into Saturn's magnetosphere (see Ip, 1997). Knowledge about the composition of their atmospheres can provide information about the surface composition (Johnson and Sittler, 1990). In the case of Dione the leading hemisphere is brighter than the trailing hemisphere (Morrison et al., 1984) which suggests darkening by plasma and energetic particle bombardment. There is also evidence of a global tectonic system of fractures and faults for Dione (Morrison et al., 1984). In the case of Enceladus fractured and smooth plains dominate which indicates its surface is relatively young $\sim 10^8$ years (Morrison et al., 1984). Enceladus is also associated with Saturn's E ring whose brightness peaks at Enceladus' L shell (Baum et al., 1981). The evidence for tectonic activity for both bodies could indicate the presence of, for example, a water-ammonia eutectic which melts at 170°K within the interior of these bodies (Morrison et al., 1984). The close encounters planned for these bodies by Cassini will provide accurate measurements of the plasma and energetic

particle populations at these bodies. This data, when combined with the latest laboratory measurements of the sputtering processes (Johnson, 1990; Johnson, 1998; Baragiola et al., 1999) can provide accurate models of their sputtered atmospheres at the time of the encounters.

Saturn's icy satellites are different than our moon since their surfaces are made of ice and energetic heavy ions will have sputtering yields ~ 50 to $1000 H_2O$ mol/ion (Johnson, 1990). Because of the large yields, trace refractory species are expected to be carried off with the water molecules. Although some information about the icy satellite composition can be acquired at large distances, the detected species will be partially equilibrated and dissociated and, therefore, the origins difficult to determine. Furthermore, when sampling the sputtering atmosphere of these bodies the freshly picked up ions will form unique ring distributions which can be readily distinguished from the ambient ions which obey bi-Maxwellian distributions. Pickup ions formed from what we call ambient neutrals will also form ring distributions, but they will have accumulated over periods ~ 10 hour rotation period of Saturn and are expected to have pitch angle scattered to shell distributions or bi-Maxwellians before being observed (see Vasylunas and Siscoe, 1976). The atmospheres of these bodies can be sampled by their conversion to ions (photoionization, electron impact ionization and charge exchange) in the form of pickup ions which can then be measured by the ion mass spectrometer (IMS) of the Cassini Plasma Spectrometer Experiment (CAPS) (see Young et al., 2002 for instrument description). The CAPS experiment will also provide measurements of the ambient plasma, ions and electrons, which will be important for estimating the charge exchange and electron impact ionization rates for the pickup ions. The Magnetospheric Imaging Instrument (MIMI) (see Krimigis et al., 2002 for instrument description) will provide the hot plasma and energetic particle observations required to estimate the sputtering rates at the time of the targeted

flybys. As discussed below the pickup ions are expected to form ring distributions which will have markedly different energy-angle properties than the ambient ions which are typically approximated by convected bi-Maxwellian distributions. We note that the pickup ions with their unique energy-angle signature can provide the most direct information about the atmosphere composition.

As discussed in Johnson and Sittler (1990) an extensively sputtered surface will display the following properties: 1) volatile species are highly depleted so trace species may be hard to detect using reflectance spectra; 2) sputtering rates for extensively sputtered surfaces are related to bulk composition hence CAPS can be more sensitive than reflectance experiment; and 3) younger surfaces such as that present at Enceladus will have higher yields. CAPS, which provides a very sensitive measurement of the icy satellites bulk atomic and molecular composition, is complementary to the information provided by the Visible Infrared Mapping Spectrometer (VIMS) (see Brown et al., 2000 for description of instrument) on Cassini which will provide spatial maps of surface composition. The Composition Infrared Spectrometer (CIRS) experiment on Cassini (see Kunde et al., 2002 for instrument description) will provide temperature maps of the icy satellite surfaces which will be important for estimating sputtering rates which are temperature dependent (see Johnson, 1990 and Bar-Nun et al., 1985).

Here we note that Pioneer 11 and Voyager 1 observations show that there may be a strong interaction between Dione and Saturn's magnetosphere which is also supported by the simulations presented in this paper. For example, Pioneer 11 (Smith and Tsurutani, 1983) and Voyager 1 (Barbosa, 1993) magnetometer observations showed the presence of ion cyclotron waves in the vicinity of Dione's L shell and the frequency of the waves are consistent with the dominant pickup ion being a heavy ion such

as H_2O^+ , OH^+ or O^+ . These waves, which are observed to be confined close to the equatorial plane, provide indirect evidence for the formation of pickup ions in the vicinity of Dione. Galileo results (Russell and Huddleston, 2000; Russell et al., 2000) show that peaks in the magnetometer spectra give information about the composition of the pickup ions being produced at a satellite body and will thus complement the CAPS observations. If the interaction is strong enough then the pickup process will also generate an ion beam instability (Ma et al., 1987) in the plasma. Such instabilities produce a spectrum of electric and magnetic waves which can be measured by the Radio and Plasma Wave Science (RPWS) instrument on Cassini (see Gurnett et al., 2000 for instrument description). If the satellite has a conductive interior then there may be a magnetic signature which could be measured by Cassini as was the case for Galileo at Europa and Callisto (see, Kivelson et al., 2000; Zimmer et al., 2000). Since the discovery of an internal magnetic field at the Jovian satellite Ganymede (Kivelson et al., 1998) we cannot rule out the presence of an internal magnetic field which would complicate the interaction and infer the presence of a dynamo operating in the core of the icy satellite. Although we think this unlikely Cassini would be able to measure the presence of such a field if present and the flyby were close enough to the icy satellite. Finally, we note that the satellites are not expected to have significant conductive ionospheres and that the atmosphere (ionosphere) is optically thin and will not be able to prevent the flowing plasma from reaching the surface of the icy satellites. The importance of these observations during targeted flybys of these various bodies by Cassini, emphasizes the need for wake encounters as close as possible to the icy satellite. This will maximize the science return from these targeted flybys which will become clearer in later discussions.

2. CAPS Instrument Description and Capabilities with Respect to Targeted Icy Satellite Encounters

The overall capabilities of the CAPS instrumentation are described in detail by Young et al. (2002). The CAPS instrument is composed of an Ion Mass Spectrometer (IMS), Electron Spectrometer (ELS) and an Ion Beam Spectrometer (IBS). With regard to the targeted icy satellite encounters the primary instruments are IMS and ELS. Here we focus our discussion on the IMS. Papers describing the IMS in detail can be found in McComas and Nordholt (1990), McComas et al. (1998) and Nordholt et al. (1998). Basically, the IMS uses time-of-flight technology with cylindrical geometry providing an instantaneous 2D view of the plasma over an angular range of 160° ; the angular resolution is $8.3^\circ \times 20^\circ$. The energy resolution $\Delta E/E \sim 17\%$. The spectrometer has a medium mass resolution feature ($M/\Delta M \sim 8$) called straight through, ST, and a high mass resolution feature ($M/\Delta M \sim 60$) using linear electric field technique, LEF, which can also be referred to as an isochronous (time focusing) technique. The present estimates of the IMS geometric factors are $G \sim 10^{-3} \text{ cm}^2\text{-ster-eV/eV}$ for ST feature and $G \sim 10^{-4} \text{ cm}^2\text{-ster-eV/eV}$ for LEF feature. We will assume these values for our simulations. CAPS also has an actuator which allows the IMS to have nearly 2π coverage in about 3 minutes ($1^\circ/\text{sec}$ scan rate). During the targeted flybys with an equatorial pass we recommend the collimator plane to be in the equatorial plane of Saturn and have the actuator dither above and below this plane to look for pitch angle scattering of the pickup ions which are expected to have ring distributions.

The relatively large geometric factor for CAPS allows it to detect ambient and pickup ions with high sensitivity. By combining ST and LEF measurements and using the mass deconvolution capabilities of the IMS Spectrum Analyzer Module (SAM) (see Sittler, 1993) the IMS will be able to resolve the water group ions (H_2O^+ , OH^+ , and H_3O^+), organics such as CH_4^+ ,

NH_3^+ , molecular oxygen O_2^+ , ozone O_3^+ , and other species such as MgO^+ . For example, a standard M/Q analyzer would not be able to distinguish between O^+ and CH_4^+ , but because of the non-linear characteristics of the LEF technique the CH_4^+ ion will breakup in the carbon foil and the C^+ ion exiting the foil will appear near the atomic C^+ ion TOF position but shifted in TOF enough to allow it to be resolved by the IMS. Our simulations, which are based on calibration data, will demonstrate this effect.

With the collimator in the equatorial plane and with an instrument energy-per-charge (E/Q) sweep time of 4 seconds ($1 \text{ eV} \leq E/Q \leq 42 \text{ keV}$ with logarithmically spaced 63 E/Q steps), CAPS should be able to provide 52 km spatial resolution of the pickup ions. Telemetry limitations confine our measurements of the dominant ambient and pickup ions to only 7 ions. But, CAPS has the ability to alternate between 7 different ion species after each energy sweep and thus provide the sampling up to 14 ions, every 8 seconds. But, in addition to the ion data (i.e., 7 to 14 ion species with full energy and pitch angle coverage), the IMS will also provide TOF versus E/Q spectrograms for both ST and LEF data (i.e., data summed over 64 E/Q sweeps and collapsed in angle for high sensitivity so no angular information is available in this data set). This data set will allow us to detect both major and minor ions with very high sensitivity. The time resolution of this data set is about 4 minutes or an equivalent spatial resolution of about 3,000 km, which is much larger than the dimensions of either Dione and Enceladus. Therefore, this data set provides no spatial information. We will present simulations of both data products in the form of 2D energy-angle contours of ion count rate for dominant ion species and some minor ion species and 2D E/Q versus TOF contours of ion counts for all ion species used in our model calculations. The ion count rate data is referred to as A cycle data, while the E/Q versus TOF data is referred to as B cycle data. An A cycle data product is composed of 8 E/Q sweeps and for the highest data

rate there will be 8 A cycles per B cycle. Each A cycle is 32 seconds long, while a B cycle is 4 minutes long.

3. Model of Sputtered Atmospheres for Dione and Enceladus

In order to construct a model of the sputtered atmospheres for either Dione or Enceladus one needs the total sputtering source rate and the energy spectrum of the sputtered neutrals. For simplicity we assume spherical symmetry, but before the actual targeted flybys we will consider models which include asymmetries due to ion Mach number, ion and electron pressure anisotropies and spatial in-homogeneities of the satellite surfaces. The latter can be temperature maps, surface properties that the imagers might detect and possible compositional spatial variations that VIMS might detect. A Monte Carlo calculation of the sputtered atmosphere including asymmetries caused by Saturn's gravitational field should also be carried out. However, to obtain preliminary estimates of the molecular species to be detected by CAPS we will use a simple spherically symmetric formula given in Johnson (1990) (see also Watson, 1982 and Sieveka, 1983). For this calculation we could use the energy spectrum for the sputtered neutrals assuming planar binding (i.e., $f(E, \cos\theta) = 4UE\cos\theta/(E+U)^3$) and spherical binding (i.e., $f(E, \cos\theta) = 2U\cos\theta/(E+U)^2$), for which we refer to Johnson (1990). For our calculations we will use the formula assuming spherical binding where U is a parameter related to the mean energy of the sputtered neutrals. U is also referred to as the chemical binding energy of the particles in the satellite surface and at present is not known with high accuracy.

For our source term S we will use the maximum sputtered flux estimated in Jurac et al. (2001) for both Dione and Enceladus. In their calculations they included the enhancements due to finite gyro-radius effects (i.e., effective satellite area) and angular enhancement caused by the $\sec\varphi$ dependence of the sputtered flux where φ is the

angle of incidence of the impacting ion relative to the normal of the satellites surface. Jurac et al. (2001) also included the photo sputter flux term. Therefore, the sputter satellite source rates are $S_D = 9.6 \times 10^{25}$ mol/s and $S_E = 2.1 \times 10^{25}$ mol/s for Dione and Enceladus, respectively.

Our sputtered atmospheric model assumes, (Jurac et al. (2001)), that the incident ion flux is dominated by heavies (i.e., O^+) and that the dominant sputtered neutral is water molecules. We will include additional species in our model atmosphere: H_2 , O_2 , CO_2 and NH_3 at the 10% level relative to the sputtered flux for water. H_2 and O_2 are direct sputter products due to energetic ion bombardment of ice (Johnson, 1990). CO_2 has been seen by the Galileo spacecraft to be an atmospheric constituent at Callisto (Carlson, 1999) and NH_3 has been suggested as a volatile in the Saturnian satellites because of Titan (Stevenson, 1982). Since the ejection of trace species is temperature dependent (Johnson, 1990; Brown et al. (1982)) and depends on the satellite composition the choice of 10% is for convenience. For example, abundance of the minor species such as CH_4 and NH_3 could be lower at the few % level. These results can then be scaled based on more detailed knowledge or new observations. However, the results given here should allow the reader to determine the ability of CAPS to detect the minor species for either of the targeted flybys. We could also have included CH_4 but since the surfaces are oxidizing we felt that having CO_2 was more appropriate.

In Figures 1 and 2 we show the result of our model calculations for Dione and Enceladus, respectively, which shows neutral density plotted as a function of height relative to the surface. In these calculations we used $U = 0.055$ eV for H_2O , CO_2 and NH_3 , while for H_2 and O_2 we use $U = 0.01$ eV. For both bodies the maximum water molecule density is about 10^5 mol/cm³ at their surfaces. In the case of Dione the next most important neutral near the surface is O_2 , while far from Dione, in order of importance, we have CO_2 , NH_3 , and H_2 . In the case of

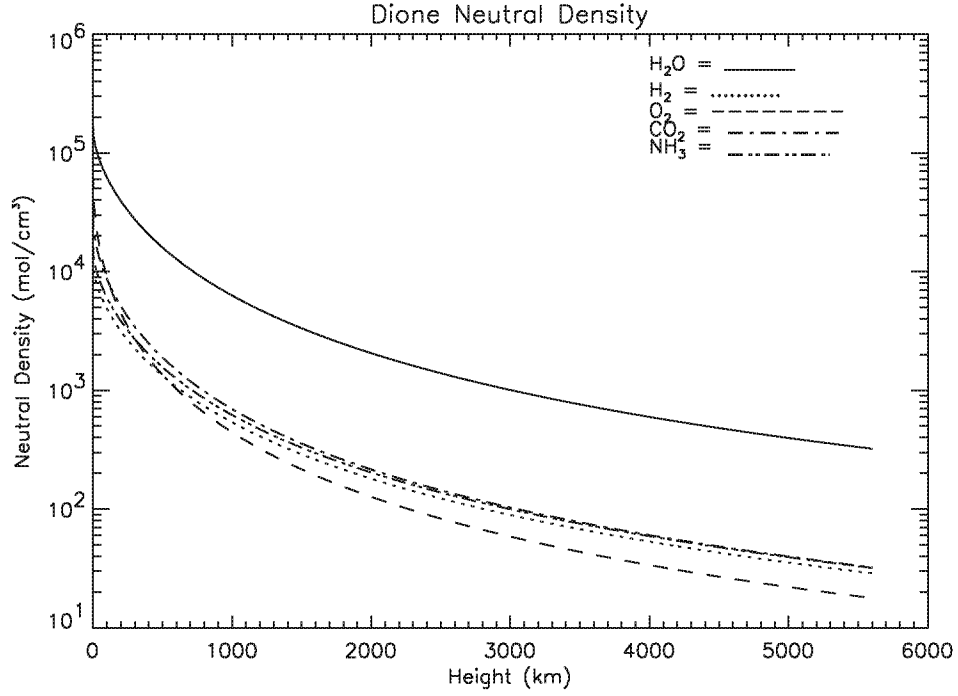


Figure 1. Computed neutral densities of Dione's sputtered atmosphere as a function of height. Assumed species are H_2O , H_2 , O_2 , CO_2 and NH_3 . The latter four species are minor and assumed to be 10% of water.

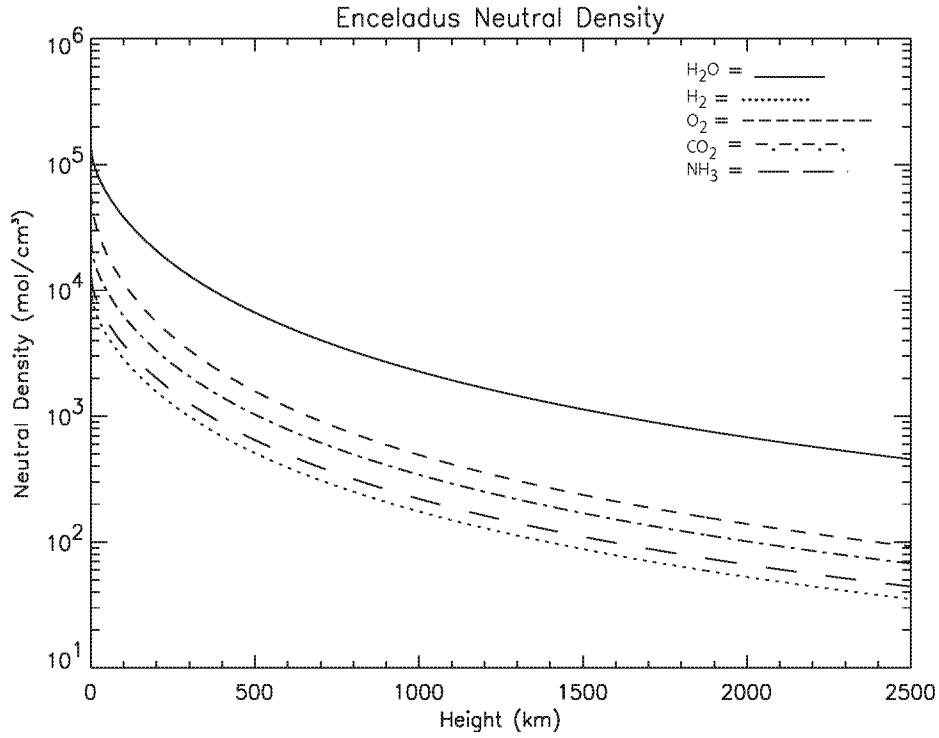


Figure 2. Computed neutral densities of Enceladus' sputtered atmosphere as a function of height. Assumed species are H_2O , H_2 , O_2 , CO_2 and NH_3 . The latter four species are minor and assumed to be 10% of water.

Enceladus, O_2 dominates relative to all the other minor species for all heights. For the remaining minor species in order of importance, we have CO_2 , NH_3 and H_2 . To some degree the variation of the neutral atmospheric density with height can be traced to the assumed energy spectrum of the sputtered neutrals and the parameter U . With 4 second time resolution, CAPS should be able to measure the height variation of the neutrals from the pickup ion measurements which will then allow us to estimate U for the different neutral species. Deviations from spherical symmetry are expected for radial distances \sim Hill Lagrange Sphere which has radius $5.7 R_{Dione}$ (i.e., 3,192 km) for Dione and $3.4 R_{Enceladus}$ (i.e., 850 km for Enceladus). For this paper, we will ignore these corrections but when we do the full Monte Carlo calculations we will include the effects of Saturn's gravity field.

4. Estimates of Pickup Ion Densities as a function of Height for Dione and Enceladus

4.1 Wake Pass

In Figure 3 we show an assumed targeted flyby geometry where the spacecraft passes through the satellite's co-rotational wake at an unspecified height $H = (\alpha \cdot r_0)$ at closest approach. The reduction of this distance will enhance CAPS ability to detect the pickup ions since they will have less time to pitch angle scatter and spread out in phase space (Wu and Davidson, 1972; Hartle and Wu, 1973). Pitch angle scattering will tend to transform a ring distribution into a shell distribution (Vasyliunas and Siscoe, 1976) which will spread the ions in velocity space and make the measured fluxes lower at a particular energy. Also, pitch angle scattering will tend to make the ions move along the magnetic field line and thus dilute the pickup ion flux in coordinate space. The net effect is to reduce our ability to measure the pickup ions. An optimal

height for a wake pass is 500 km since it is optimal for the Cassini remote sensing instruments because of the spacecraft's ability to turn in order to remove smearing effects and close enough to measure ring distributions by CAPS. The figure also shows a fluid element as it passes through the satellite's atmosphere to the observation point where the spacecraft is located. As the fluid element moves through the atmosphere it will collect pickup ions as the neutral atmosphere is ionized by charge exchange reactions (Table 1), electron impact ionization reactions (Table 2) and photo-ionization reactions (Table 3). In order to compute the pickup ion densities correctly we will also need estimates of the ambient densities and temperatures of the ions and electrons in the vicinity of Dione and Enceladus which are given in Table 4. Table 4 also gives the ambient densities of the various neutral components at Dione and Enceladus. All the numbers in Table 4 were derived from the papers by Richardson et al. (1986) and Richardson et al. (1998). Since our model calculations use a fluid approximation we are ignoring the finite gyro-radius effects of the pickup ions. In the case of Dione the gyro-radius for H_2O^+ is about 123 km which is small relative to a Dione radius (560 km) and at Enceladus the gyro-radius for H_2O^+ is about 20 km which is much less than the radius of Enceladus (250 km). So, to a good approximation the fluid approximation should be accurate. Deviations from this will occur on the side facing Saturn where the pickup ions can gyrate into the body's surface for heights less than the ion gyro-radius. So, for heights near the satellite's surface we would expect to see an asymmetry in the observed pickup ion densities. From Richardson (1986) the observed plasma velocity at Dione is about 46 km/s and at Enceladus is 33 km/s. The magnetic field strength at Dione is about 70 nT while that at Enceladus is 312 nT (see Connerney et al., 1983).

ICY SATELLITE FLYBY GEOMETRY

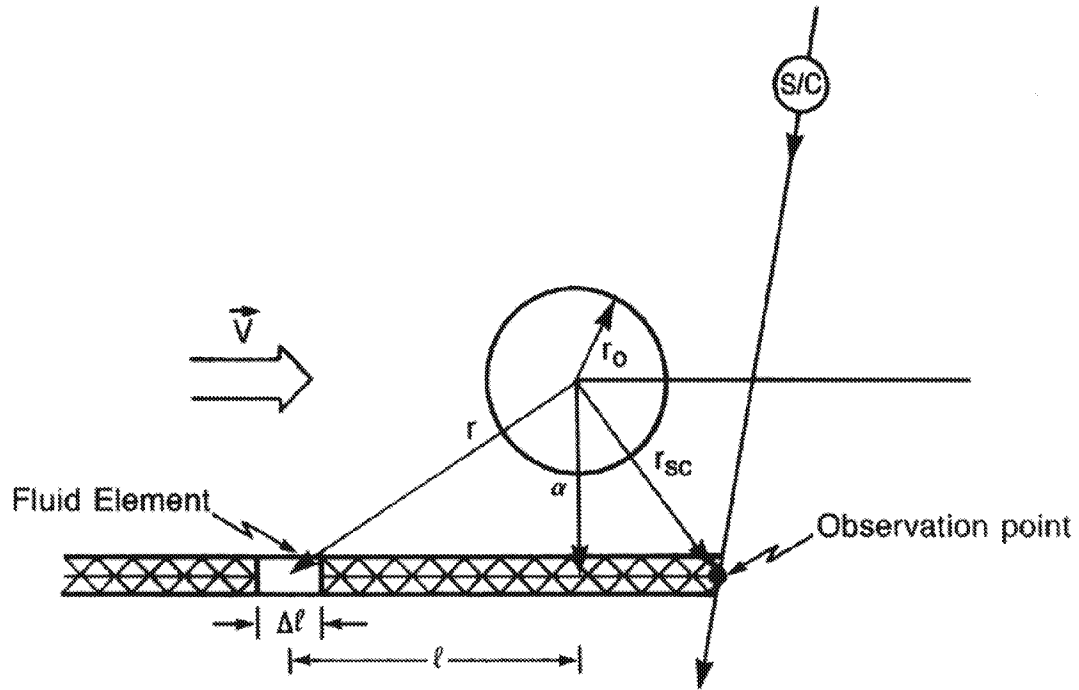


Figure 3. Shows encounter geometry and how we compute pickup ion densities as a fluid element passes through the satellites sputtered atmosphere and picks up ions as the neutrals are ionized due to photo-ionization, electron impact ionization and charge exchange reactions.

Table 1. Charge Exchange Rates

Reaction	Rates, cm ³ /s		
	Enceladus	Dione	Reference
$H^+ + H \rightarrow H + H^+$	1.5E-8	1.5E-8	<i>Neuman et al.</i> [1982]
$O^+ + H \rightarrow O + H^+$	6.2E-9	6.3E-9	<i>Stebbins and Rutherford</i> [1968]
$O^+ + OH \rightarrow O_2 + H^+$	1.2E-10	1.2E-10	<i>Giguere and Huebner</i> [1978]
$H^+ + H_2 \rightarrow H + H_2^+$	1.7E-10	1.7E-10	<i>Tawara</i> [1978]
$H_2^+ + H_2 \rightarrow H_2 + H_2^+$	6.6E-9	6.6E-9	<i>Massay and Gilbody</i> [1974]
$H^+ + H_2O \rightarrow H + H_2O^+$	5.0E-8	5.0E-8	<i>Tawara</i> [1978]
$H^+ + H_2O \rightarrow H + H_2O^+$	8.2e-9	8.2e-9	<i>Ip</i> [1997]
$O^+ + H_2O \rightarrow O + H_2O^+$	2.3E-9	2.3E-9	<i>Albritton</i> [1978]
$OH^+ + H_2O \rightarrow OH + H_2O^+$	1.6E-9	1.6E-9	<i>Huntress</i> [1977], <i>Kim et al.</i> [1974]
$OH^+ + H_2 \rightarrow H + H_2O^+$	1.1E-9	1.1E-9	<i>Huntress</i> [1977]
$H_2^+ + H_2O \rightarrow H_2 + H_2O^+$	3.9E-9	3.9E-9	<i>Huntress</i> [1977]
$OH^+ + OH \rightarrow H_2O^+ + O$	7.0e-10	7.0e-10	<i>Ip</i> [1997]
$H_2^+ + OH \rightarrow H_2O^+ + H$	7.6e-10	7.6e-10	<i>Ip</i> [1997]
$H^+ + O \rightarrow H + O^+$	5.5E-9	5.5E-9	<i>Stebbins et al.</i> [1964]
$O^+ + O \rightarrow O + O^+$	9.9E-9	9.9E-9	<i>Stebbins et al.</i> [1964]
$O_2^+ + O_2 \rightarrow O_2 + O_2^+$	6.4E-9	6.4E-9	<i>Banks and Kockarts</i> [1973]
$H_2^+ + O_2 \rightarrow H_2 + O_2^+$	9.4E-9	9.4E-9	<i>Tawara</i> [1978]
$O^+ + O_2 \rightarrow O + O_2^+$	2.1E-9	2.1E-9	<i>Albritton et al.</i> [1977]
$OH^+ + O_2 \rightarrow OH + O_2^+$	2.0E-10	2.0E-10	<i>Bortner et al.</i> [1972]
$H_2O^+ + O_2 \rightarrow H_2O + O_2^+$	5.0E-9	5.0E-9	<i>Fehsenfeld et al.</i> [1967]
$H^+ + O_2 \rightarrow H + O_2^+$	1.17E-9	1.17E-9	<i>Rudd et al.</i> [1985]
$O^+ + CO_2 \rightarrow CO + O_2^+$	1.1E-9	1.1E-9	<i>Giguere and Heubner</i> [1978]
$H^+ + OH \rightarrow H + OH^+$	3.0E-10	3.0E-10	<i>Giguere and Heubner</i> [1978]
$H^+ + OH \rightarrow H + OH^+$	2.1e-9	2.1e-9	<i>Ip</i> [1997]
$H_2^+ + O \rightarrow H + OH^+$	1.0E-9	1.0E-9	<i>Giguere and Heubner</i> [1978]
$O^+ + H_2 \rightarrow H + OH^+$	1.6E-9	1.6E-9	<i>Huntress</i> [1977], <i>Kim et al.</i> [1974]
$H_2^+ + OH \rightarrow OH^+ + H_2$	7.6e-10	7.6e-10	<i>Ip</i> [1997]
$O^+ + OH \rightarrow O + OH^+$	3.0E-10	3.0E-10	<i>Giguere and Heubner</i> [1978]
$O^+ + OH \rightarrow O + OH^+$	3.6e-10	3.6e-10	<i>Ip</i> [1997]
$O^+ + NH_3 \rightarrow NH_2 + OH^+$	2.2E-9	2.2E-9	<i>Huntress</i> [1977], <i>Oppenheimer</i> [1975]*
$O^+ + CO_2 \rightarrow O + CO_2^+$	1.1E-10	1.1E-10	<i>Rudd et al.</i> [1985]*
$H^+ + CO_2 \rightarrow H + CO_2^+$	1.1E-9	1.1E-9	<i>Rudd et al.</i> [1985]
$H^+ + NH_3 \rightarrow H + NH_3^+$	5.2E-9	5.2E-9	<i>Huntress</i> [1977]
$H_2^+ + NH_3 \rightarrow H_2 + NH_3^+$	5.7E-9	5.7E-9	<i>Huntress</i> [1977]
$OH^+ + NH_3 \rightarrow OH + NH_3^+$	1.2E-9	1.2E-9	<i>Huntress</i> [1977]
$H_2O^+ + NH_3 \rightarrow H_2O + NH_3^+$	2.2E-9	2.2E-9	<i>Huntress</i> [1977]
$H_2^+ + H_2O \rightarrow H_2 + H_3O^+$	3.4E-9	3.4E-9	<i>Huntress</i> [1977]
$OH^+ + H_2O \rightarrow O + H_3O^+$	1.3E-9	1.3E-9	<i>Huntress</i> [1977]
$H_2O^+ + H_2 \rightarrow H + H_3O^+$	6.1E-10	6.1E-10	<i>Huntress</i> [1977], <i>Kim et al.</i> [1974]
$H_2O^+ + H_2O \rightarrow OH + H_3O^+$	2.1E-9	2.1E-9	<i>Huntress</i> [1977]

*Estimated

Table 2. Electron Impact Ionization Rates

Rates, cm ³ /s			
Reaction	Enceladus	Dione	References
$H + e \rightarrow H^+ + 2e$	1.3E-10	2.45E-9	<i>Lotz [1967]</i>
$H + e^* \rightarrow H^+ + 2e$	3.1E-8	3.1E-8	<i>Lotz [1967]</i>
$H_2 + e \rightarrow H^+ + H + 2e$	7.3E-14	3.3E-11	<i>Ip [1997]</i>
$H_2 + e^* \rightarrow H^+ + H + 2e$	1.01E-8	1.92E-8	<i>Ip [1997]</i>
$H_2O + e \rightarrow H^+ + OH + 2e$	1.66E-12	7.4E-11	<i>Orient and Srivastava [1987]</i>
$H_2O + e^* \rightarrow H^+ + OH + 2e$	4.06E-8	4.35E-8	<i>Orient and Srivastava [1987]</i>
$NH_3 + e \rightarrow H^+ + NH_2 + 2e$	2.58E-14	1.79E-12	<i>Mark et al. [1977]</i>
$NH_3 + e^* \rightarrow H^+ + NH_2 + 2e$	5.28E-10	5.44E-10	<i>Mark et al. [1977]</i>
$H_2 + e \rightarrow H_2^+ + 2e$	2.26E-10	2.2E-9	<i>Kieffer [1969]</i>
$H_2 + e^* \rightarrow H_2^+ + 2e$	5.5E-8	5.5E-8	<i>Kieffer [1969]</i>
$NH_3 + e \rightarrow NH + H_2^+ + 2e$	1.35E-13	1.86E-12	<i>Mark et al. [1977]</i>
$NH_3 + e^* \rightarrow NH + H_2^+ + 2e$	9.51E-11	9.63E-11	<i>Mark et al. [1977]</i>
$H_2O + e \rightarrow H_2O^+ + 2e$	8.6E-11	8.88E-10	<i>Orient and Srivastava [1987]</i>
$H_2O + e^* \rightarrow H_2O^+ + 2e$	9.32E-8	9.3E-8	<i>Orient and Srivastava [1987]</i>
$O + e \rightarrow O^+ + 2e$	2.01E-10	2.0E-9	<i>Lotz [1967]</i>
$O + e^* \rightarrow O^+ + 2e$	8.2E-8	8.2E-8	<i>Lotz [1967]</i>
$H_2O + e \rightarrow O^+ + OH + 2e$	1.26E-13	9.72E-12	<i>Orient and Srivastava [1987]</i>
$H_2O + e^* \rightarrow O^+ + OH + 2e$	1.06E-8	1.16E-8	<i>Orient and Srivastava [1987]</i>
$CO_2 + e \rightarrow O^+ + CO + 2e$	2.17E-12	7.4E-11	<i>Orient and Srivastava [1987]</i>
$CO_2 + e^* \rightarrow O^+ + CO + 2e$	1.22E-8	1.45E-8	<i>Orient and Srivastava [1987]</i>
$O_2 + e \rightarrow O_2^+ + 2e$	2.1E-10	1.98E-9	<i>Banks and Kockarts [1973]</i>
$O_2 + e^* \rightarrow O_2^+ + 2e$	1.5E-7	1.72E-7	<i>Banks and Kockarts [1973]</i>
$OH + e \rightarrow OH^+ + 2e$	3.7E-10	3.16E-9	<i>Richardson et al. [1986]</i>
$H_2O + e \rightarrow OH^+ + 2e$	1.7E-11	3.7E-10	<i>Orient and Srivastava [1987]</i>
$H_2O + e^* \rightarrow OH^+ + 2e$	4.61E-8	4.6E-8	<i>Orient and Srivastava [1987]</i>
$CO_2 + e \rightarrow CO_2^+ + 2e$	1.73E-10	2.36E-9	<i>Orient and Srivastava [1987]</i>
$CO_2 + e^* \rightarrow CO_2^+ + 2e$	1.63E-7	1.9E-7	<i>Orient and Srivastava [1987]</i>
$CO_2 + e \rightarrow CO^+ + 2e$	4.45E-12	7.05E-11	<i>Orient and Srivastava [1987]</i>
$CO_2 + e^* \rightarrow CO^+ + 2e$	6.04E-9	6.99E-9	<i>Orient and Srivastava [1987]</i>
$CO_2 + e \rightarrow C^+ + O_2 + 2e$	9.5E-14	5.92E-12	<i>Orient and Srivastava [1987]</i>
$CO_2 + e^* \rightarrow C^+ + O_2 + 2e$	3.33E-9	3.86E-9	<i>Orient and Srivastava [1987]</i>
$NH_3 + e \rightarrow NH_3^+ + 2e$	2.66E-10	2.03E-9	<i>Mark et al. [1977]</i>
$NH_3 + e^* \rightarrow NH_3^+ + 2e$	5.23E-8	5.26E-8	<i>Mark et al. [1977]</i>
$NH_3 + e \rightarrow NH_2^+ + H + 2e$	3.85E-11	6.6E-10	<i>Mark et al. [1977]</i>
$NH_3 + e^* \rightarrow NH_2^+ + H + 2e$	4.2E-8	4.32E-8	<i>Mark et al. [1977]</i>
$NH_3 + e \rightarrow NH^+ + H_2 + 2e$	1.71E-13	9.21E-12	<i>Mark et al. [1977]</i>
$NH_3 + e^* \rightarrow NH^+ + H_2 + 2e$	1.49E-9	1.52E-9	<i>Mark et al. [1977]</i>
$NH_3 + e \rightarrow N^+ + H_2 + H + 2e$	1.33E-14	1.26E-12	<i>Mark et al. [1977]</i>
$NH_3 + e^* \rightarrow N^+ + H_2 + H + 2e$	5.44E-10	5.67E-10	<i>Mark et al. [1977]</i>

* Hot Electron Component

Table 3. Photoionization Rates

Rates, s ⁻¹		
Reaction	Enceladus-Dione	References
$\text{H} + h\nu \rightarrow \text{H}^+ + \text{e}$	8.0E-10	<i>Huebner and Giguere</i> [1980]
$\text{H}_2 + h\nu \rightarrow \text{H}^+ + \text{H} + \text{e}$	1.0E-10	<i>Huebner and Giguere</i> [1980]
$\text{H}_2\text{O} + h\nu \rightarrow \text{H}^+ + \text{OH} + \text{e}$	1.4E-10	<i>Huebner and Giguere</i> [1980]
$\text{NH}_3 + h\nu \rightarrow \text{H}^+ + \text{NH}_2 + \text{e}$	3.7E-11	<i>Huebner et al.</i> [1992]
$\text{H}_2 + h\nu \rightarrow \text{H}_2^+ + \text{e}$	5.9E-10	<i>Huebner and Giguere</i> [1980]
$\text{H}_2\text{O} + h\nu \rightarrow \text{H}_2\text{O}^+ + \text{e}$	3.7E-9	<i>Huebner and Giguere</i> [1980]
$\text{O} + h\nu \rightarrow \text{O}^+ + \text{e}$	2.3E-9	<i>Huebner and Giguere</i> [1980]
$\text{H}_2\text{O} + h\nu \rightarrow \text{O}^+ + \text{H}_2 + \text{e}$	6.4E-11	<i>Huebner and Giguere</i> [1980]
$\text{O}_2 + h\nu \rightarrow \text{O}^+ + \text{O} + \text{e}$	5.8E-10	<i>Huebner and Giguere</i> [1980]
$\text{CO}_2 + h\nu \rightarrow \text{O}^+ + \text{CO} + \text{e}$	2.8E-10	<i>Huebner et al.</i> [1992]
$\text{O}_2 + h\nu \rightarrow \text{O}_2^+ + \text{e}$	5.6E-9	<i>Huebner and Giguere</i> [1980]
$\text{OH} + h\nu \rightarrow \text{OH}^+ + \text{e}$	3.7E-9	<i>Huebner and Giguere</i> [1980]
$\text{CO}_2 + h\nu \rightarrow \text{CO}_2^+ + \text{e}$	2.6E-9	<i>Huebner et al.</i> [1992]
$\text{CO}_2 + h\nu \rightarrow \text{CO}^+ + \text{O} + \text{e}$	1.68E-10	<i>Huebner et al.</i> [1992]
$\text{CO}_2 + h\nu \rightarrow \text{C}^+ + \text{O}_2 + \text{e}$	1.2E-10	<i>Huebner et al.</i> [1992]
$\text{NH}_3 + h\nu \rightarrow \text{NH}_3^+ + \text{e}$	6.8E-9	<i>Huebner et al.</i> [1992]
$\text{NH}_3 + h\nu \rightarrow \text{NH}_2^+ + \text{H} + \text{e}$	1.96E-9	<i>Huebner et al.</i> [1992]
$\text{NH}_3 + h\nu \rightarrow \text{NH}^+ + \text{H}_2 + \text{e}$	7.66E-11	<i>Huebner et al.</i> [1992]
$\text{NH}_3 + h\nu \rightarrow \text{N}^+ + \text{H}_2 + \text{H} + \text{e}$	3.6E-11	<i>Huebner et al.</i> [1992]

Table 4. Enceladus Torus

Steady State Densities (cm ⁻³)												
N _{ce}	N _{he}	H	H ⁺	H ₂ ⁺	O	O ⁺	OH	OH ⁺	H ₂ O	H ₂ O ⁺	O ₂	O ₂ ⁺
100.0	0.2	50	25	0.265*	100	50	500	10	100	15	0.0	0.03*
Steady State Ion Electron Temperatures (eV)												
T _{ce}	T _{he}	T(H ⁺)	T(H ₂ ⁺)*	T(O ⁺)	T(OH ⁺)**	T(H ₂ O ⁺)**	T(O ₂ ⁺)**					
3.0	100	11	22	80	85	90	160					

Dione Torus

Steady State Densities (cm ⁻³)												
N _{ce}	N _{he}	H	H ⁺	H ₂ ⁺	O	O ⁺	OH	OH ⁺	H ₂ O	H ₂ O ⁺	O ₂	O ₂ ⁺
25.4	0.4	80	4.6	0.81*	180	11.8	250	4.45	30	3.6	0.0	0.15*
Steady State Ion Electron Temperatures (eV)												
T _{ce}	T _{he}	T(H ⁺)	T(H ₂ ⁺)*	T(O ⁺)	T(OH ⁺)**	T(H ₂ O ⁺)**	T(O ₂ ⁺)**					
5.5	145	16.5	33	105	111	118	210					

* Richardson et al. (1986)

** Assume temperature proportional to ion mass.

The results of our pickup ion densities as a function of height for a wake pass is shown in Figures 4a and 4b for Dione and Figure 5a and 5b for Enceladus. We arbitrarily set the closest approach distance equal to the satellite radius (i.e., 560 km for Dione and 250 km for Enceladus). Referring to Figure 4a for Dione the H_2O^+ densities reach peak values of about 1.0 ions/cm³ near the surface. H_2^+ has the lowest density, while H^+ and O_2^+ have peak densities of about 0.06 ions/cm³ and 0.08 ions/cm³, respectively. Pickup O^+ is relatively low in abundance relative to ambient densities and will probably be difficult to detect since the dominant ambient ion is expected to be O^+ . The relatively flat profile for O^+ at all heights except near the surface indicates we are primarily seeing pickup ions produced by ambient neutral oxygen. Figure 4b shows pickup ion densities at Dione for OH^+ , CO_2^+ , NH_3^+ , H_3O^+ and NH_2^+ . Within 560 km in height all ions should be detectable. OH^+ dominates relative to the other ions in this figure and surprisingly, H_3O^+ is relatively abundant. Near Dione's surface the total pickup ion density is about 1.4 ions/cm³ which is about 5.6% the ambient density and we may expect to see a modest interaction at Dione. Here we note that because of the detection of ozone, O_3 , at

Dione (Noll et al., 1997) we may see significant fluxes of pickup O_2^+ and O_3^+ within a few hundred kms above Dione's surface and therefore a strong interaction similar to that observed by Voyager 1 at Titan (Neubauer et al., 1984).

In the case of Enceladus H_2O^+ clearly dominates over all other ions with peak densities near the surface of 2.2 ions/cm³. The next most important ion is O_2^+ with peak densities near 0.15 ions/cm³ at the surface. The other ions H^+ , O^+ and H_2^+ are of low abundance and will only be detectable close to the bodies surface. Again, because of the high abundance of ambient H^+ and O^+ , pickup H^+ and O^+ will be undetectable. In Figure 5b the ions H_3O^+ , OH^+ , CO_2^+ and NH_3^+ should all be detectable. The ion NH_2^+ may be detectable close to Enceladus' surface. Here we are using as a rule of thumb for CAPS ability of detection of 0.001 ions/cm³ for ST data and 0.01 ions/cm³ for LEF data. This will become more apparent when we show our ring distribution simulations.

Figures 4 and 5 also show the height variation of the pickup ion densities and as mentioned previously this height variation will allow us to infer something about the energy distribution of the sputtered neutrals.

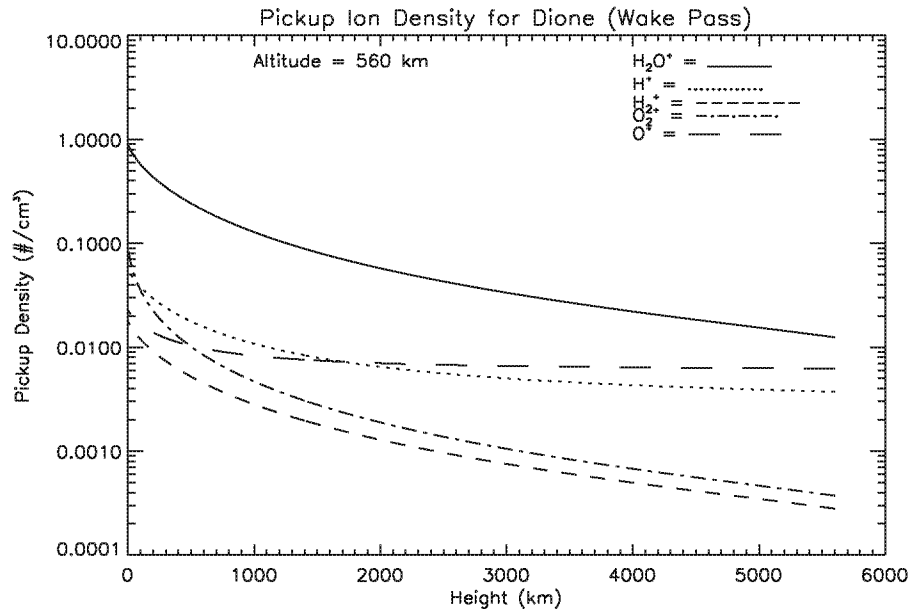


Figure 4a. Computed ion densities at spacecraft for Dione wake flyby as a function of height for H_2O^+ , O_2^+ , H_2^+ , O^+ and H^+ ions. The height is equal to the $a - r_0$ parameter in Figure 3.

Figure 5a. Computed ion densities at spacecraft for Enceladus wake flyby as a function of height for H_2O^+ , O_2^+ , H_2^+ , O^+ and H^+ ions. The height is equal to the $a - r_0$ parameter in Figure 3.

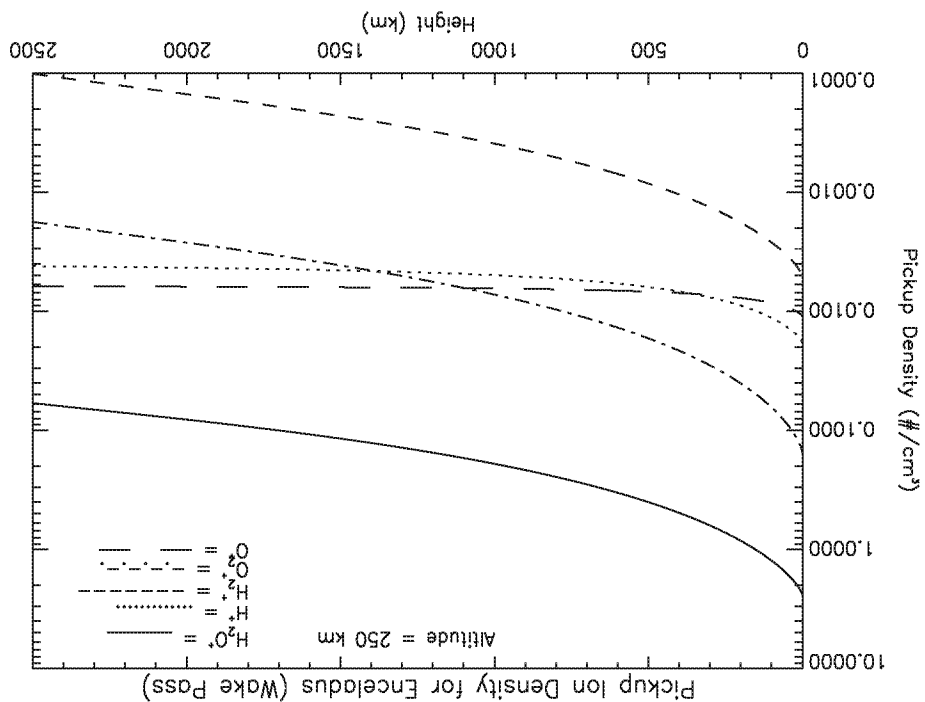
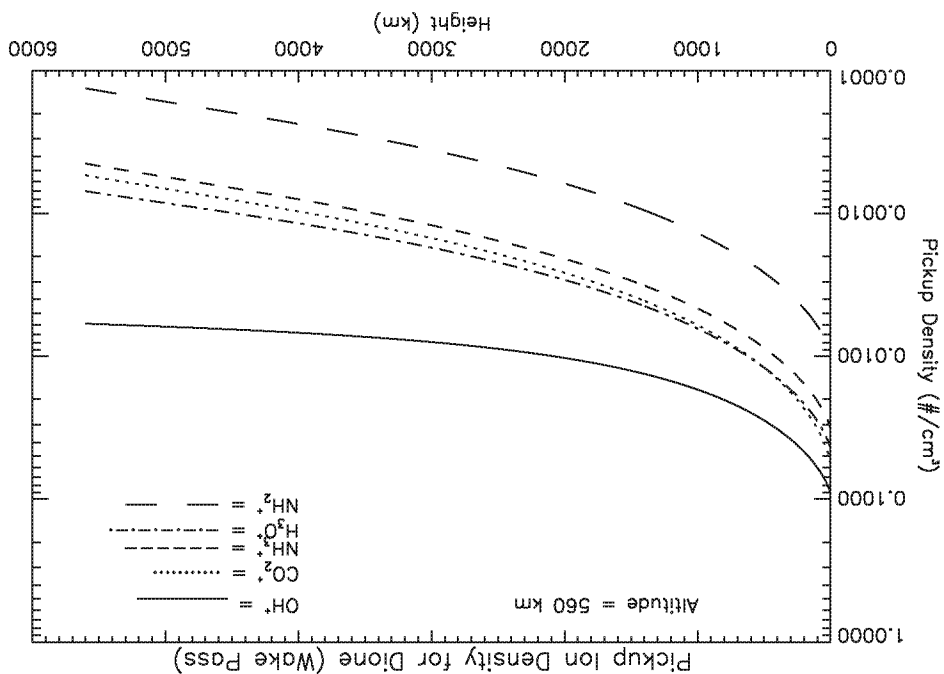


Figure 4b. Computed ion densities at spacecraft for Dione wake flyby as a function of height for OH^+ , CO_2^+ , NH_3^+ , NH_2^+ and H_3O^+ . The height is equal to the $a - r_0$ parameter in Figure 3.



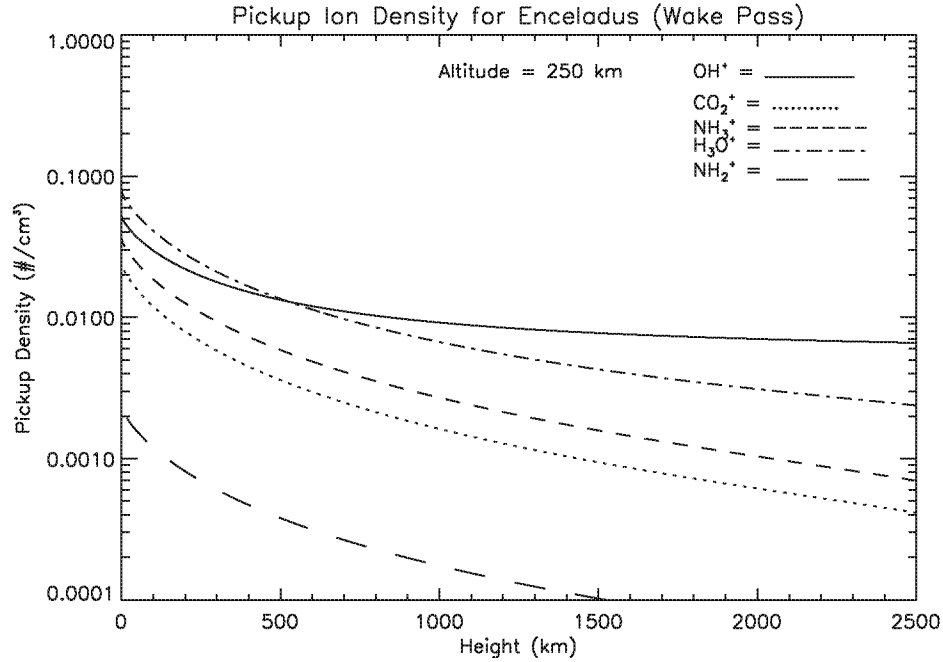


Figure 5b. Computed ion densities at spacecraft for Enceladus wake flyby as a function of height for OH^+ , CO_2^+ , NH_3^+ , NH_2^+ and H_3O^+ . The height is equal to the $a - r_0$ parameter in Figure 3.

4.2 Upstream Passes

In Figures 6a and 6b we show the pickup ion density as a function of distance Y for an upstream pass with closest approach altitude of 500 km for Dione. Y is the distance along the spacecraft trajectory relative to the center of the body (i.e., $Y = 0$ corresponds to closest approach). In the case of H_2O^+ we have detectable pickup ion fluxes for the ion measurements by CAPS. The H_2^+ and O_2^+ measurements are also possible for pickup ions since we can use the ST measurements for them. H^+ and O^+ pickup ions will be undetectable because of the relatively high ambient densities of these species. Referring to Figure 6b we see that OH^+ (LEF detection), CO_2^+ (ST detection) pickup ion detection is clearly possible while H_3O^+ (LEF detection) detection is very marginal at closest approach and probably not possible. If we use ST data for OH^+ and H_3O^+ detection will be difficult since ambient O^+ and H_2O^+ will dominate. NH_3^+ (LEF detection) is not possible.

In Figures 7a and 7b we show the pickup ion density as a function of distance Y for an upstream pass with closest approach altitude of 100 km for Dione (i.e., for navigation reasons such a close encounter is not allowed but shown to compare upstream pass versus wake pass). Here, H_2O^+ (ST detection), O_2^+ (ST detection), and H_2^+ (ST detection) pickup ion detection are possible out to several thousand kilometers. H^+ and O^+ pickup ions are not detectable because of high ambient densities for these ion species. In Figure 7b ions, OH^+ (LEF detection), and CO_2^+ (ST detection) are possible to detect in the ion data out to 1000 km for all. To detect NH_3^+ and H_3O^+ we would need LEF detection but then their peak densities would have to exceed 0.01 ions/cm³. NH_2^+ (LEF detection) pickup ion detection is not possible. The point should be made that we are assuming 10% abundance, while the abundances could be a few % or less; then detection for many of the minor species will probably not be possible.

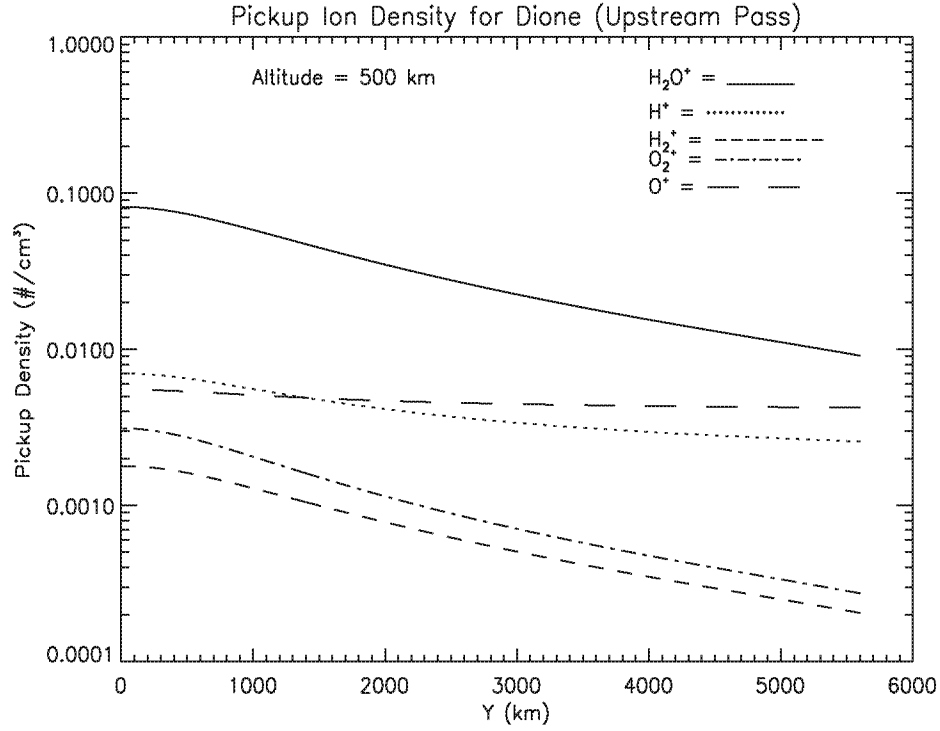


Figure 6a. Computed ion densities at spacecraft for Dione upstream pass as a function of transverse distance $Y = a$ (see Figure 3) with 500 km closest approach altitude for H_2O^+ , O_2^+ , H_2^+ , O^+ and H^+ ions.

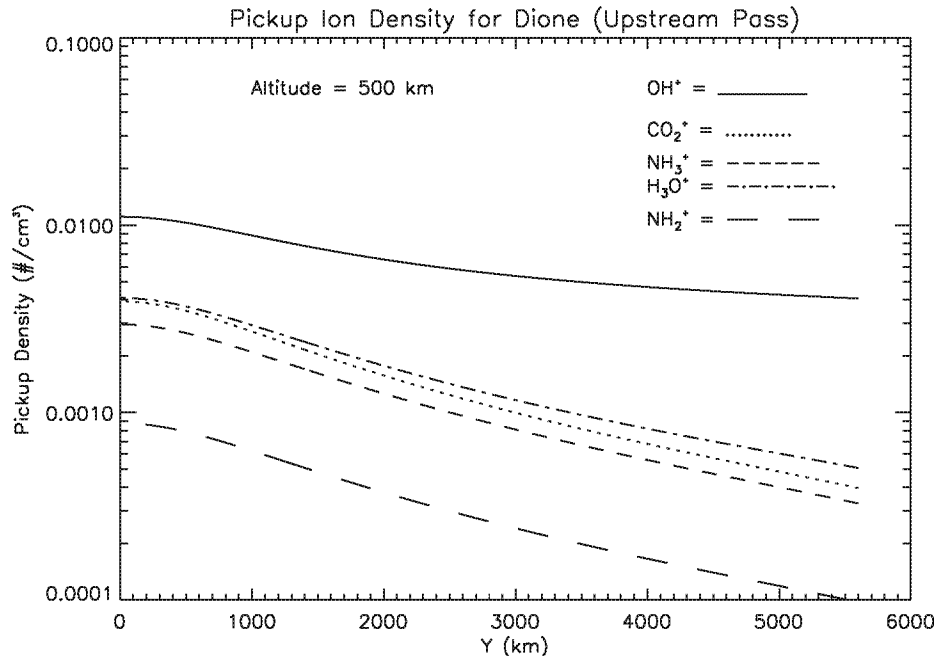


Figure 6b. Computed ion densities at spacecraft for Dione upstream pass as a function of transverse distance $Y = a$ (see Figure 3) with 500 km closest approach altitude for OH^+ , CO_2^+ , NH_3^+ , NH_2^+ and H_3O^+ ions.

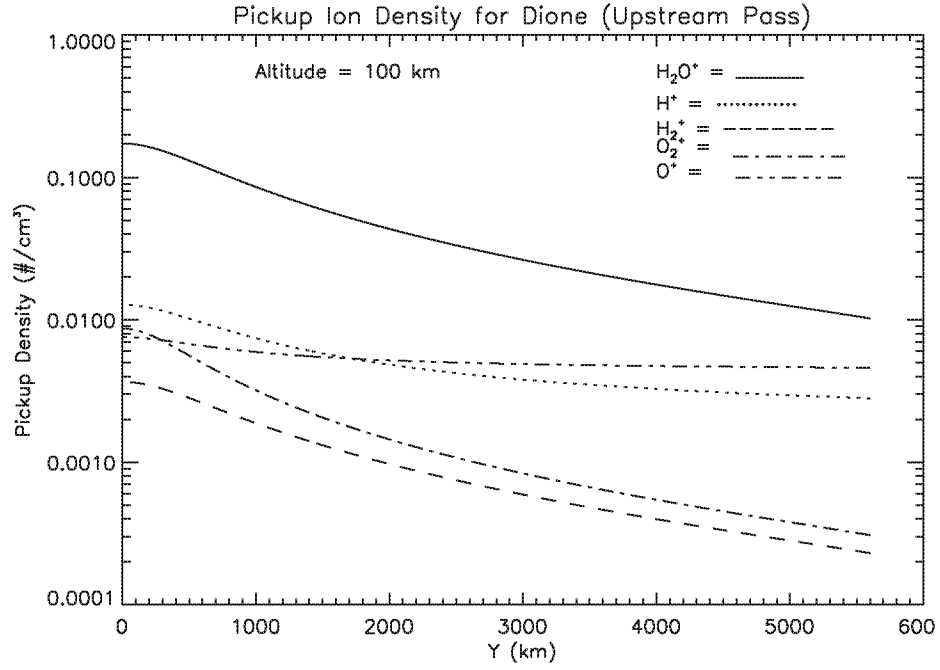


Figure 7a. Computed ion densities at spacecraft for Dione upstream pass as a function of transverse distance $Y = a$ (see Figure 3) with 100 km closest approach altitude for H_2O^+ , O_2^+ , H_2^+ , O^+ and H^+ ions.

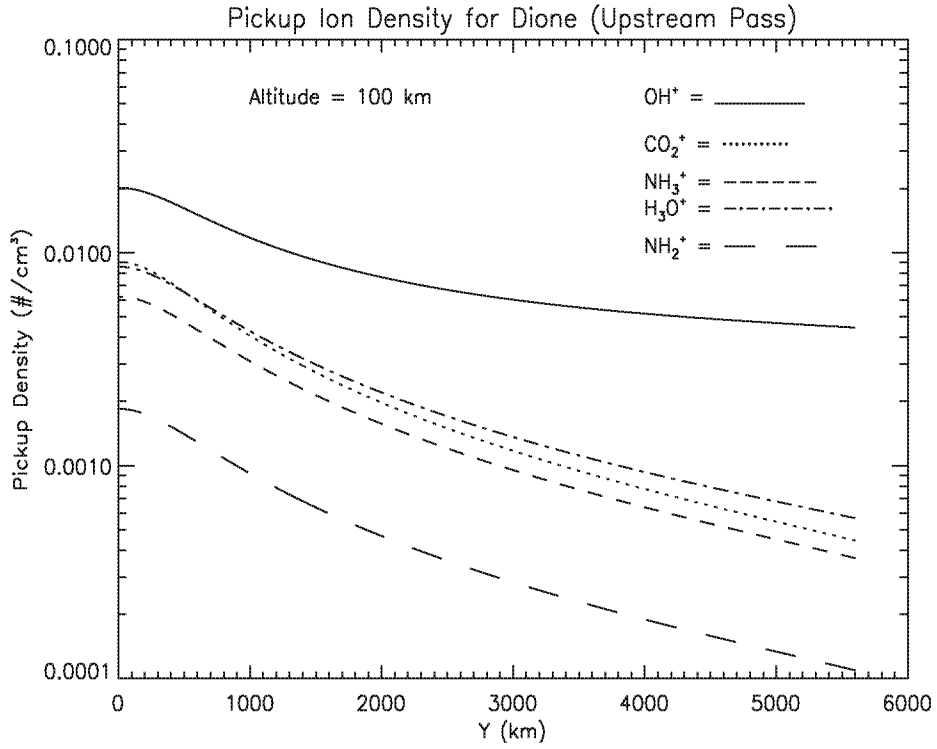


Figure 7b. Computed ion densities at spacecraft for Dione upstream pass as a function of transverse distance $Y = a$ (see Figure 3) with 100 km closest approach altitude for OH^+ , CO_2^+ , NH_3^+ , NH_2^+ and H_3O^+ ions.

In Figures 8a and 8b we show the pickup ion density as a function of distance Y for an upstream pass with closest approach altitude of 500 km for Enceladus. In Figure 8a H_2O^+ (ST detection), and O_2^+ (ST detection) pickup ion detection at all altitudes are possible. H_2^+ (ST detection) pickup ion detection is not possible at all heights. H^+ and O^+ are not detectable because of the high ambient

densities of these species. In Figure 8b, OH^+ (LEF detection), H_3O^+ (LEF detection) and NH_3^+ (LEF detection) of pickup ions are below the detection threshold of the instrument. We could try and detect OH^+ and H_3O^+ using ST data but will need to compete with ambient O^+ and H_2O^+ . NH_2^+ is not detectable.

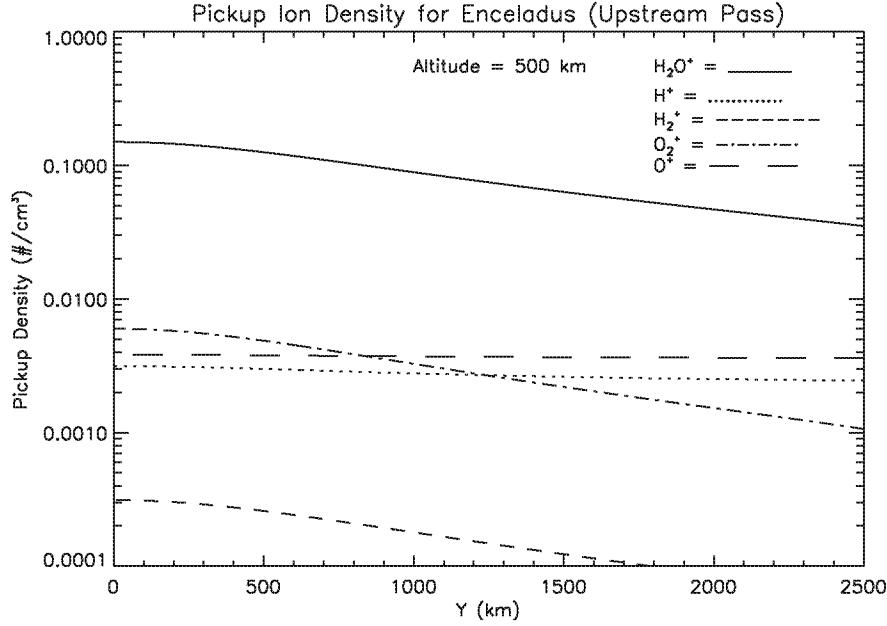


Figure 8a. Computed ion densities at spacecraft for Enceladus upstream pass as a function of transverse distance $Y = a$ (see Figure 3) with 500 km closest approach altitude for H_2O^+ , O_2^+ , H_2^+ , O^+ and H^+ ions.

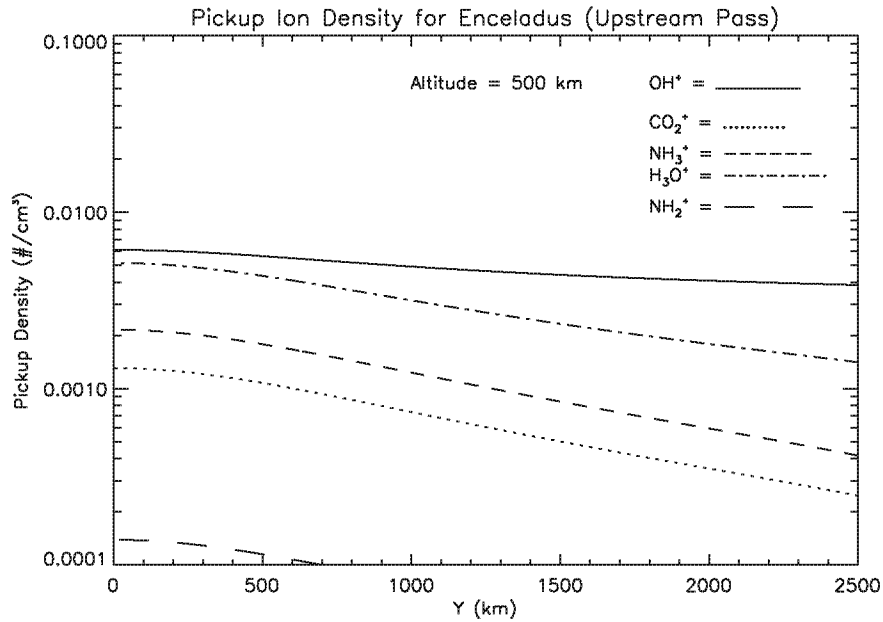


Figure 8b. Computed ion densities at spacecraft for Enceladus upstream pass as a function of transverse distance $Y = a$ (see Figure 3) with 500 km closest approach altitude for OH^+ , CO_2^+ , NH_3^+ , NH_2^+ and H_3O^+ ions.

In Figures 9a and 9b we show the pickup ion density as a function of distance Y for an upstream pass with closest approach altitude of 100 km for Enceladus (i.e., here again a flyby distance of 100 km is not allowed because of navigation issues but is shown to compare upstream passes versus wake passes). In Figure 9a H_2O^+ (ST detection), and O_2^+ (ST detection) pickup ion detection is possible at all distances. H_2^+ (ST detection) pickup ion detection is not possible. The detection of H^+ and O^+ pickup ion detection is not possible because of the large ambi-

ent ion densities for these species. In Figure 9b, OH^+ (LEF detection) and H_3O^+ (LEF detection) pickup ion detection may be possible inside 1000 km; if we use ST data instead their detection may be possible at all heights, but then they have to compete with ambient O^+ , OH^+ and H_2O^+ . NH_3^+ (LEF detection) pickup ion detection is not possible at all heights. CO_2^+ (ST detection) pickup ion detection is possible at all heights. NH_2^+ (ST or LEF detection) pickup ion detection is not possible at all heights.

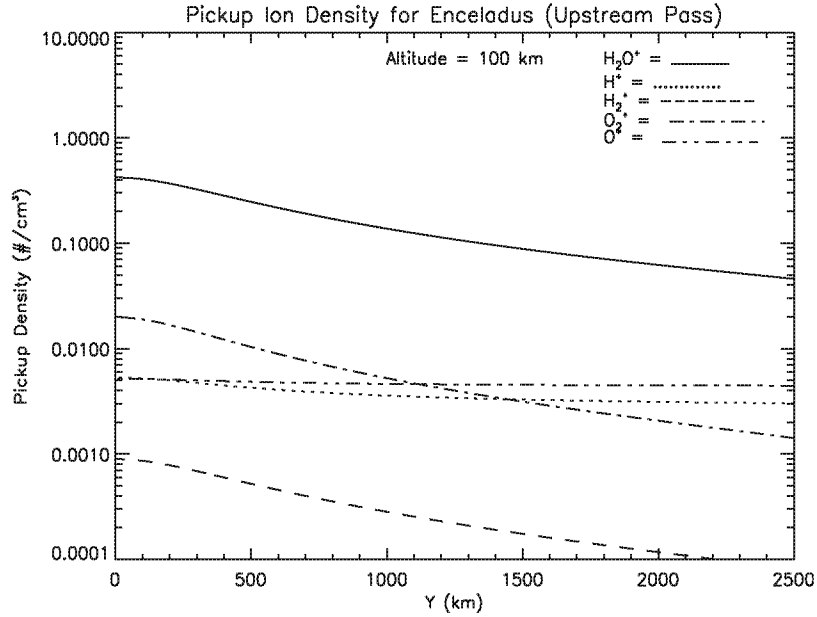


Figure 9a. Computed ion densities at spacecraft for Enceladus upstream pass as a function of transverse distance $Y = a$ (see Figure 3) with 100 km closest approach altitude for H_2O^+ , O_2^+ , H_2^+ , O^+ and H^+ ions.

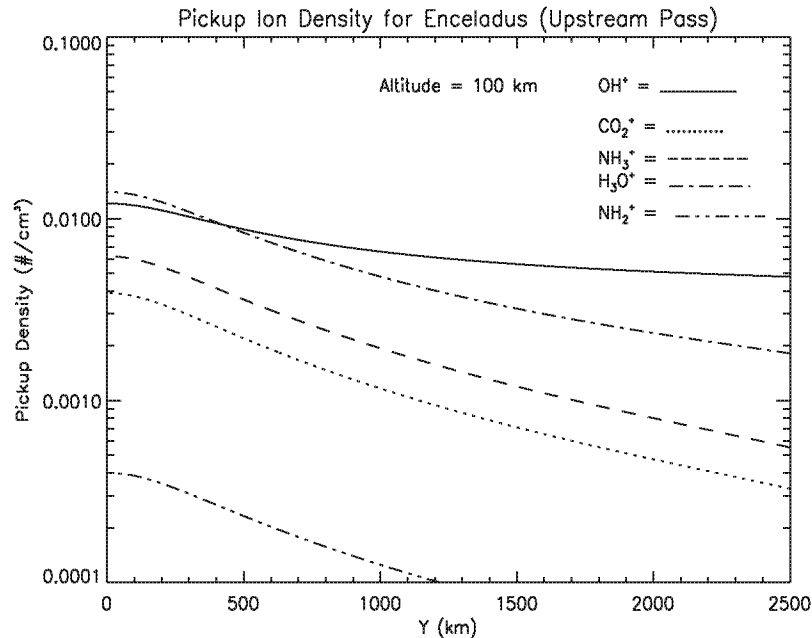


Figure 9b. Computed ion densities at spacecraft for Enceladus upstream pass as a function of transverse distance $Y = a$ (see Figure 3) with 100 km closest approach altitude for OH^+ , CO_2^+ , NH_3^+ , NH_2^+ and H_3O^+ ions.

At this point we would like to add the following caveat that many of the minor ions for which detection using either ST or LEF data was ruled out as not being detectable referred to the ion count measurements or A cycle data, while with regard to the B cycle data, which is considerably more sensitive, we may be able to detect these minor ions. But, such detection would provide minimal information about the pitch angle distributions of the various ion species which is needed to distinguish between ambient ions and pickup ions which are expected to be in the form of ring distributions.

5. Ring Distribution Simulations

Here we derive the expressions used to compute the simulated ion count rates for CAPS of the pickup ions. These calculations assume that the ions are in the form of a ring distribution and have not had sufficient time to pitch angle scatter before they are observed by CAPS (see Wu and Davison, 1972 and Hartle and Wu, 1973). In the plasma frame of reference one can write the velocity distribution for a fresh pickup ion (Hartle and Wu, 1973)

$$f(\vec{v}^*) = \frac{n}{2\pi v_{0\perp}} \delta(\vec{v}_{\perp}^* - \vec{v}_{0\perp}) \delta(v_z^* - v_{0z})$$

\vec{v}^* the particle velocity in the plasma frame with \vec{v}_0 the mean velocity of the plasma which will be in the direction of co-rotation. The component perpendicular to the magnetic field is indicated by the symbol \perp and the component along the magnetic field is along the z axis. One can then re-write the above expression in the appropriate form when viewed in the spacecraft frame ignoring for now spacecraft motion

$$f(\vec{v}) = \frac{n}{4V_x} \delta(v_z) \left[\delta(v_y - \sqrt{2v_x V_x - v_x^2}) + \delta(v_y + \sqrt{2v_x V_x - v_x^2}) \right]$$

where V_x is the flow speed of the ambient ions with x along the co-rotation direction. \vec{v} is the velocity of the pickup ion in the spacecraft frame. Finally, this expression can be further reformulated into a more useful form

$$f(\vec{v}) = \frac{n}{2\pi \sqrt{2v_x V_x}} \delta(v_r - \sqrt{2v_x V_x}) \delta(v_z)$$

In Figure 10 we show a schematic of the ring distribution in the spacecraft frame. We are now in a position to incorporate this expression in the equation defining the observed count rate for a given distribution function $f(\vec{v})$. The general expression for the count rate that CAPS would observe is

$$CR = \epsilon A \iint_{\Delta v \Delta \Omega} R(E/Q, \theta, \phi; \vec{v}) f(\vec{v}) \vec{v} \cdot \hat{n} v_r dv_r dv_z d\phi$$

for which $R(E/Q, \theta, \phi; \vec{v})$ is the response function of the IMS with E/Q the tuned energy-per-charge of the IMS, θ the angle relative to the collimator normal of the IMS and ϕ the angular sector of the IMS. This equation reduces to the following expression after substituting the above expression for f

$$CR = \frac{\epsilon A n \sqrt{2v_x V_x} \Delta \phi}{2\pi}$$

Here, ϵ represents the detection efficiency of the IMS, A is its effective area of detection, and $\Delta \phi$ is the angular width of the IMS angular sectors which are $\sim 20^\circ$. We then introduce the geometric factor $G = \epsilon A \Delta \Omega \Delta E / E \approx 10^{-3} \text{ cm}^2 \text{-ster-eV/eV}$ from which we get

$$CR = \left(\frac{G}{\Delta \Omega \Delta E / E} \right) \left(\frac{n \Delta \phi}{2\pi} \right) \left(\sqrt{2v_x V_x} \right)$$

for which $\Delta \Omega = 0.05 \text{ ster}$, $\Delta E/E = 0.17$, and $0 \leq v_x \leq 2V_x$. In the limit of $v_x = 2V_x$ and setting $V_x \approx 50 \text{ km/s}$ we get

$$CR = 1.2 \times 10^5 n \text{ cps.}$$

for ST data where n is the density of the pickup ion in units of ions/cm³. So, it can be seen that modest densities can produce very high count rates in CAPS if we sample the ring distribution function before it can pitch angle scatter and spread out in phase space.

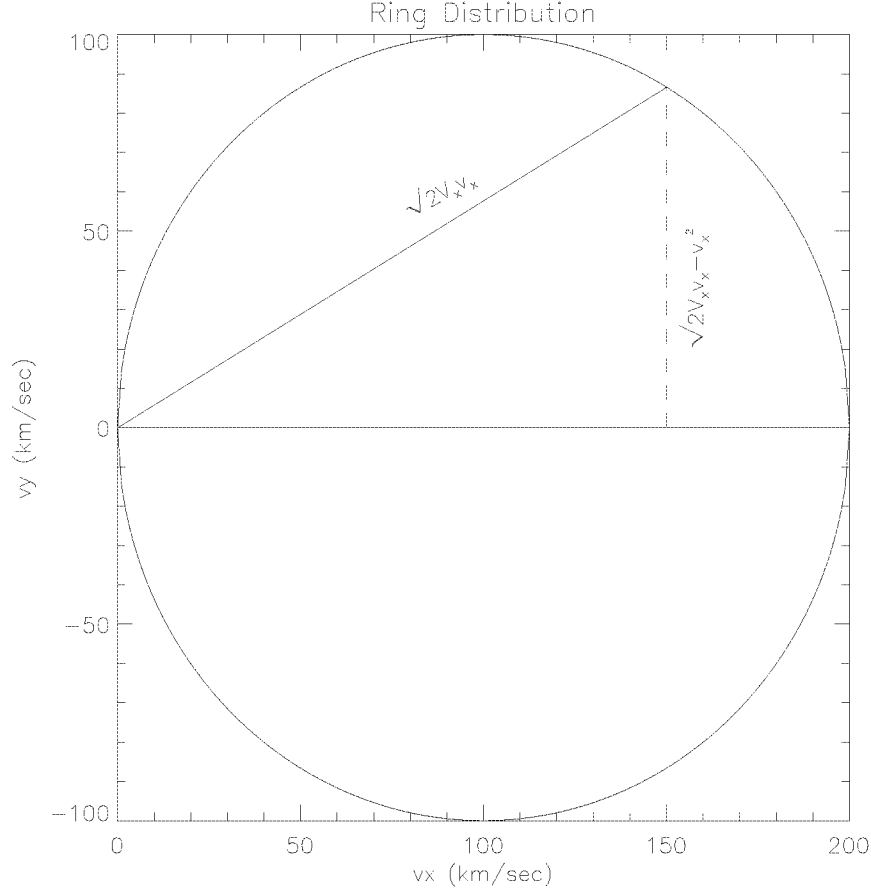


Figure 10. Ring velocity distribution for pickup ions with drift speed V_x .

Simulations of the pickup ions plus ambient ions for various species are shown in Figure 11 for Dione and Figure 12 for Enceladus (i.e., A cycle data) for which we assumed for Dione densities of 1.0 ions/cm³ for H₂O⁺, 0.08 ions/cm³ for O₂⁺, 0.06 ions/cm³ for CO₂⁺, and 0.03 ions/cm³ for NH₃⁺ and for Enceladus we assumed densities of 2.2 ions/cm³ for H₂O⁺, 0.15 ions/cm³ for O₂⁺, 0.025 ions/cm³ for CO₂⁺, and 0.04 ions/cm³ for NH₃⁺. These pickup ion densities were derived from our wake pass calculations at zero height. For the ambient ions we assumed convected Maxwellians and used the ion parameters in Table 4. For reference we show the energy-angle coverage provided by CAPS in Figure 13 a and

13b for O₂⁺ at Dione and Enceladus, respectively. It should be clear from Figures 11, 12 and 13 that in most cases CAPS will be able to measure the ring distributions of the pickup ions for such species as H₂O⁺, O₂⁺, CO₂⁺, and NH₃⁺ during a wake pass. This should also be true for some of the other ion species such as OH⁺ and H₃O⁺. As can be seen that the count rates can exceed several 100 kHz for the pickup ions and in many cases should allow us to see them many 1000 of kilometers above the satellites surface. Here, we note that for the molecule NH₃⁺ we will need to use LEF data, so the displayed counts in Figure 11d and 12d will be an order of magnitude lower for LEF data.

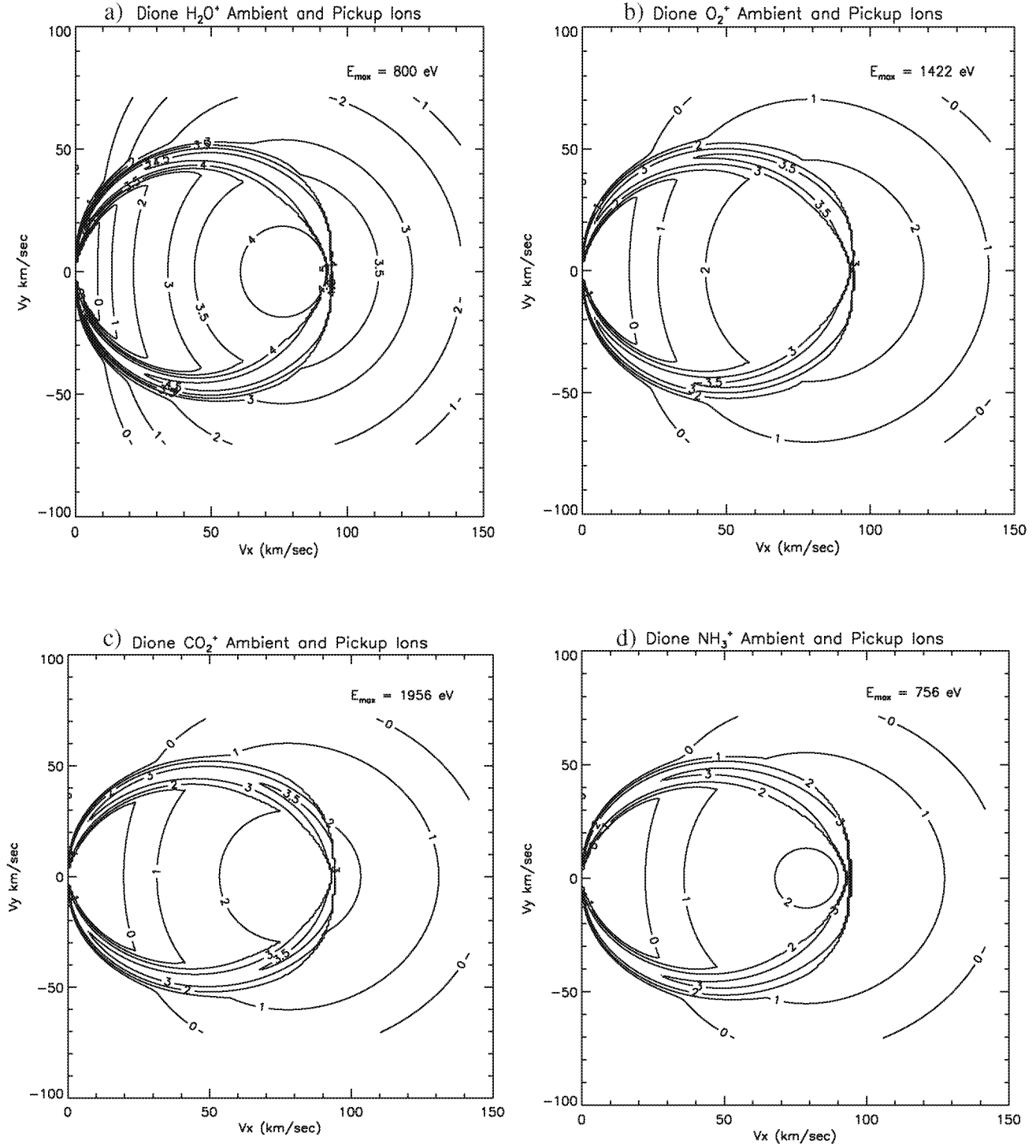


Figure 11. Contour plots of simulated ion count rate at Dione for a) H_2O^+ , b) O_2^+ , c) CO_2^+ and d) NH_3^+ .

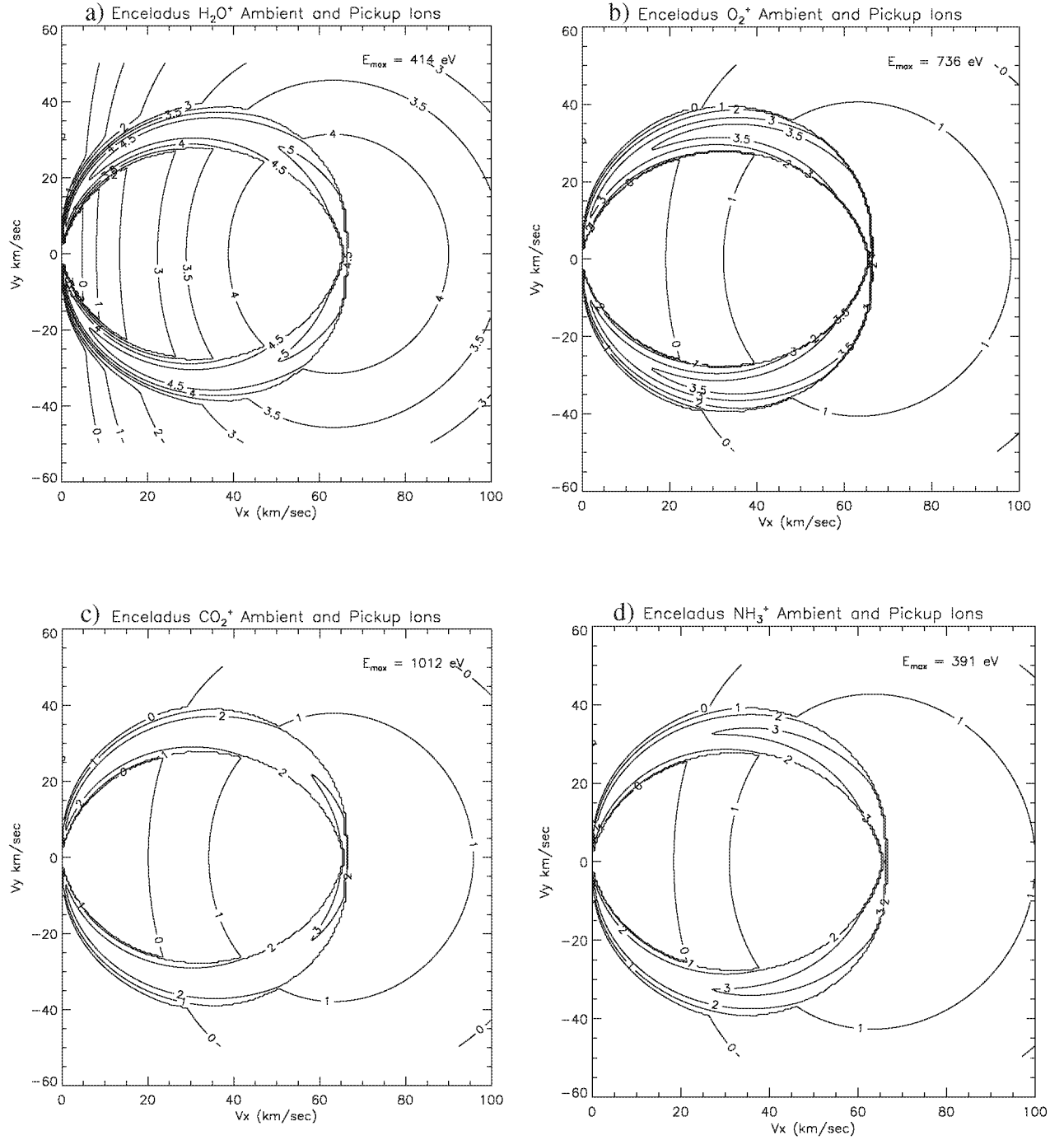


Figure 12. Contour plots of simulated ion count rate at Enceladus for a) H_2O^+ , b) O_2^+ , c) CO_2^+ and d) NH_3^+ .

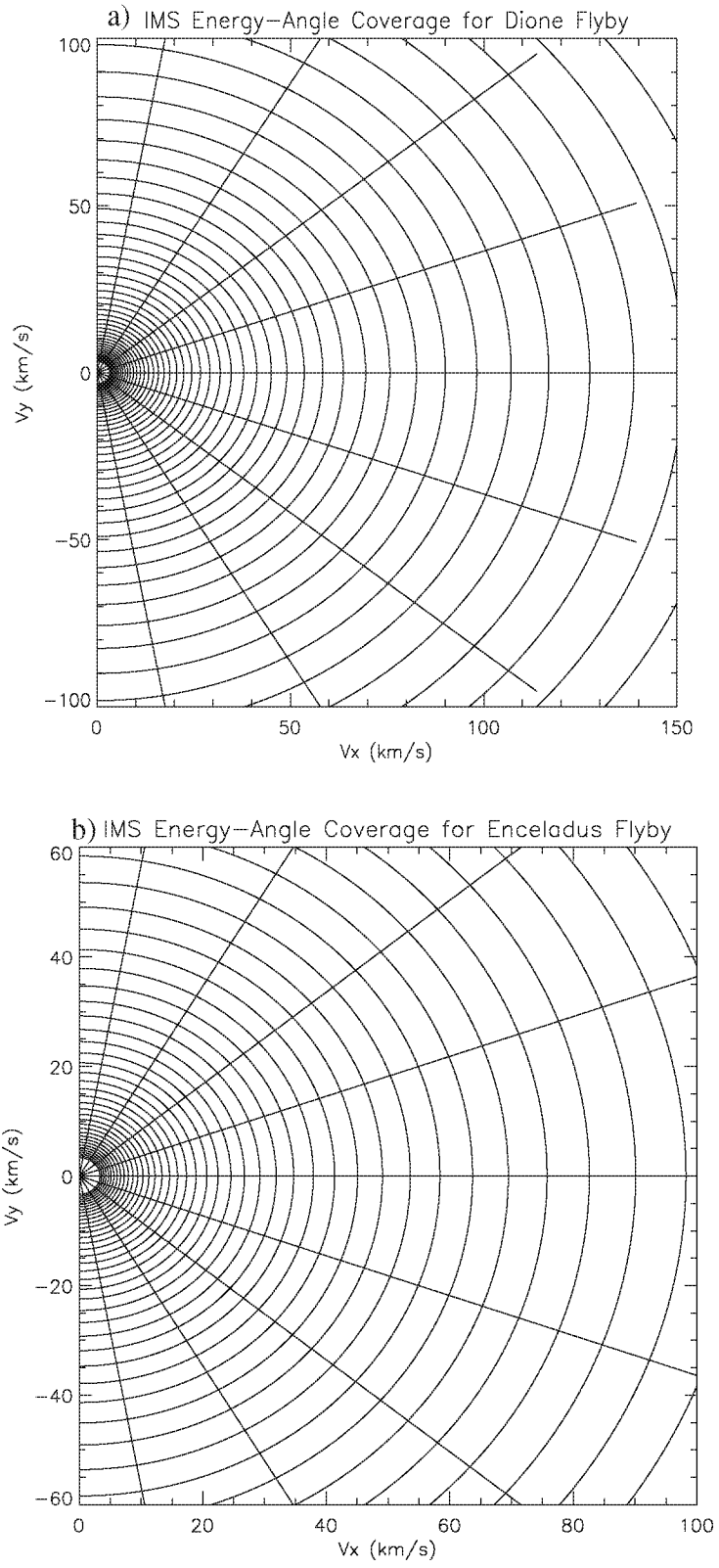


Figure 13. Example plot of IMS energy-angle coverage for pickup ions at a) Dione and b) Enceladus.

6. Simulated E/Q Versus TOF Spectrograms

We are now in a position to compute simulated E/Q versus TOF contour plots of ion counts for both ST and LEF data (i.e., B cycle data) for a wake pass only. These simulations will require us to integrate along the spacecraft trajectory over distances ~ 3000 km. Therefore, this data set will not provide information about the radial variation of the ion density or information about the pitch angle distributions. Considering the time and spatial scales of each encounter we will get one spectrum before closest approach and one spectrum after closest approach. But, the advantage of this data set is that it provides the energy spectrum of each ion species detected and because of its higher sensitivity and observed TOF spectrum allows us to detect the minor ions more easily and detect unexpected ion species. The results of these simulations are shown in Figure 14a and 14b for Dione and Figure 15a and 15b for Enceladus. We display the data using the full energy range of the spectrometer where we have added nearby energy steps as done for the B cycle data (i.e., 32 E/Q steps). Note, that the spectrograms are plotted versus TOF channel number for which each channel is about 0.75 nsec wide. We have also added Poisson statistical noise to the data and accounts for its variable nature.

Some caveats with regard to the ST simulations are required to be said. First, for the H^+ and H_2^+

data we have ignored the importance of the H⁻ fragment, which can exit the carbon foil; this fragment is relatively small when compared to the neutral H fragment. At present we do not have reliable C⁺ calibration data and are using appropriately shifted N⁺ calibration data for our C⁺ ions; here we are ignoring the C⁻ fragment for incident C⁺ ions. For NH⁺ we are also using appropriately shifted N⁺ calibration data so that the H⁻ fragment is being ignored. For the remainder of the species O⁺ calibration data is predominately used and this calibration data was contaminated with methane, which was evidently in the calibration facilities ion source. So, this data had C⁻ and H⁻ fragments. In cases of OH⁺, H₂O⁺ and H₃O⁺ we kept the H⁻ fragment but deleted the C⁻ fragment. For O⁺ and O₂⁺ we deleted the H⁻ and C⁻ fragments. For NH₃⁺ we deleted the C⁻ and O⁻ fragments, while for CO₂⁺ and CO⁺ we deleted the H⁻ fragment. At present the relative abundance of methane and oxygen in the ion source is not known so there is some intrinsic error in the relative heights of the different fragments for the various species. At this time these minor corrections do not impact the goals of this paper, but are issues to be dealt with when it comes to the final calibration of the instrument (i.e., using prototype and engineering versions of flight unit) and operation of the instrument within Saturn's magnetosphere and surrounding solar wind.

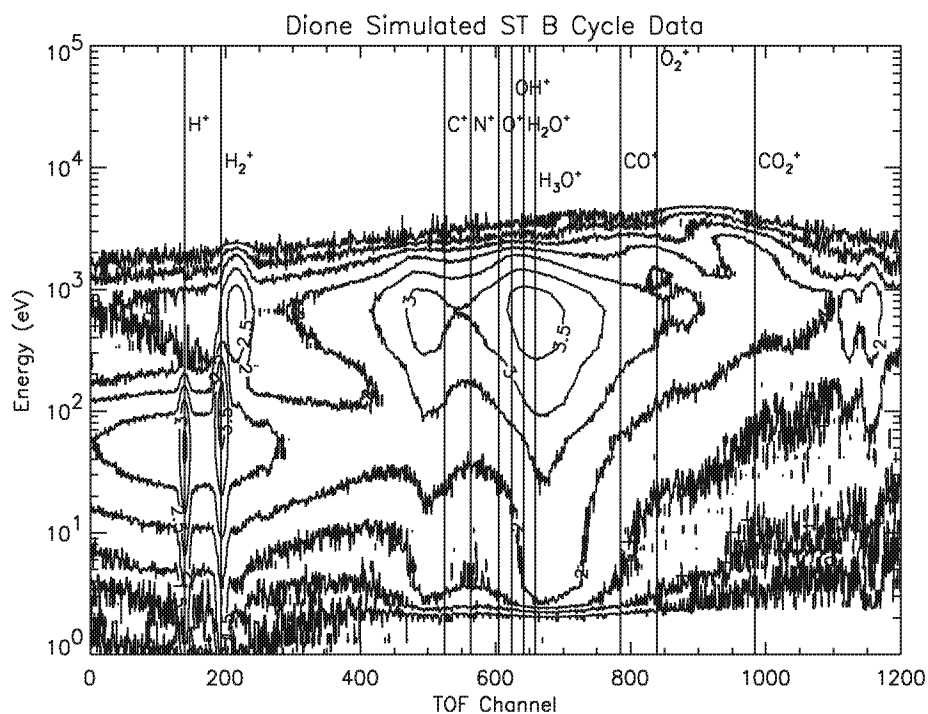


Figure 14a. Energy versus time-of-flight (TOF) contour map of simulated ions counts for B cycle ST data for Dione wake pass encounter. Vertical lines give approximate peak positions for various incident ions.

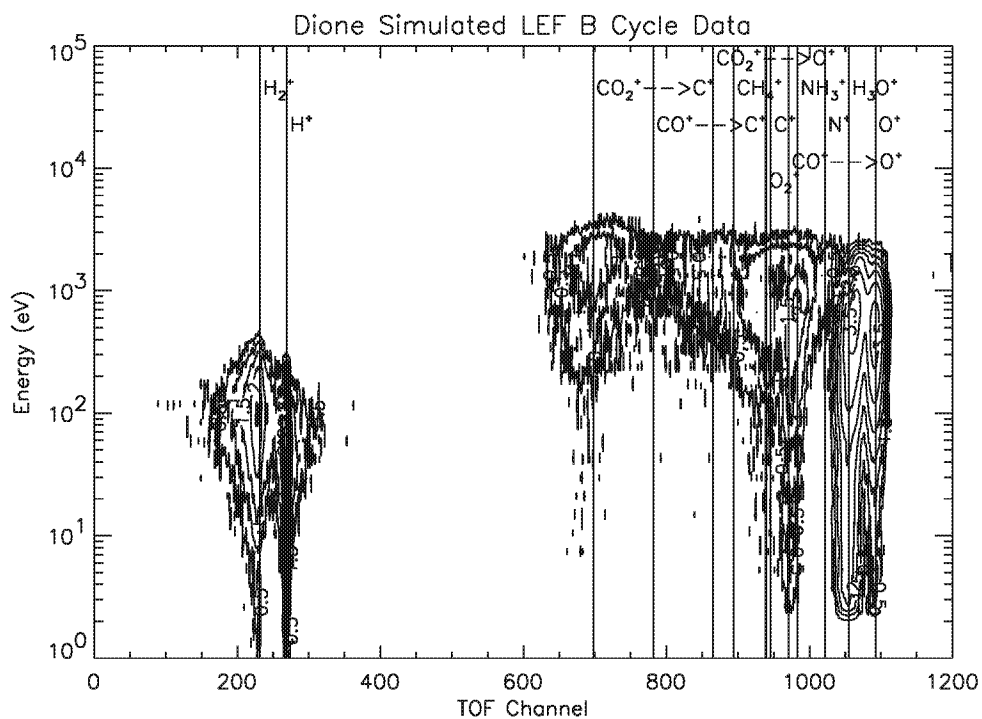


Figure 14b. Energy versus time-of-flight (TOF) contour map of simulated ions counts for B cycle LEF data for Dione encounter. Vertical lines give approximate peak positions for various incident ions.

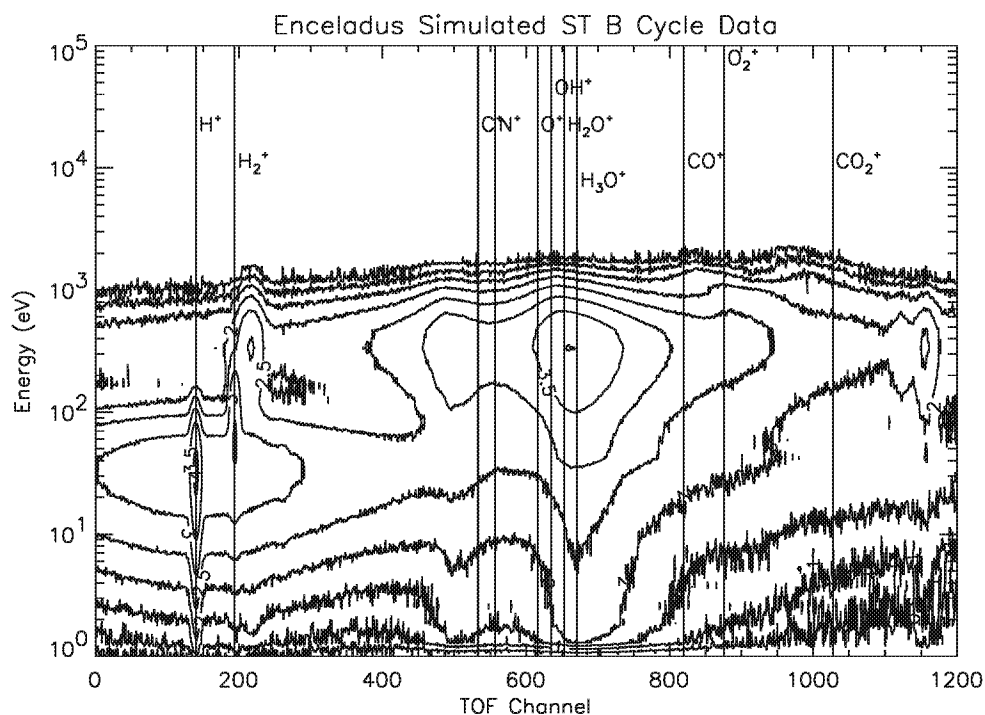


Figure 15a. Energy versus time-of-flight (TOF) contour map of simulated ions counts for B cycle ST data for Enceladus encounter. Vertical lines give approximate peak positions for various incident ions.

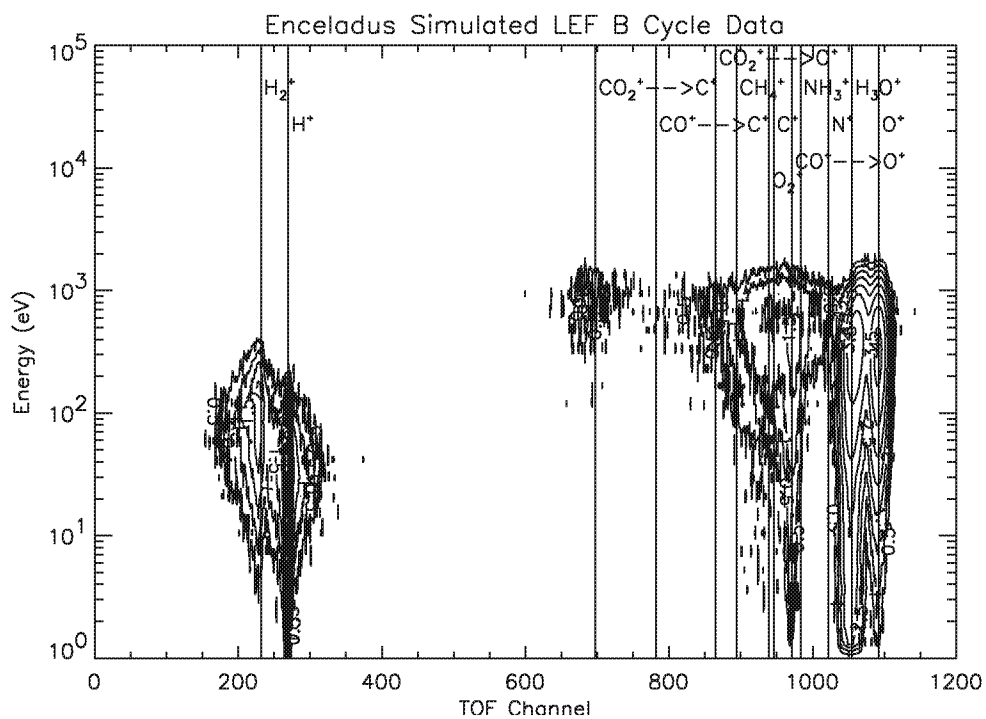


Figure 15b. Energy versus time-of-flight (TOF) contour map of simulated ions counts for B cycle LEF data for Enceladus encounter. Vertical lines give approximate peak positions for various incident ions.

The simulations of the ST data in Figures 14a and 15a show that we can resolve the H^+ and H_2^+ in the ST data for which the H_2^+ extend to higher energy because of its greater mass. The same can be said for the water group ions being separated from both O_2^+ (i.e., note that in the ST data O_2^+ cannot be distinguished uniquely from S^+) and CO_2^+ , respectively, in the ST data. One can also see that the accumulated counts for the water group ions can exceed 10^4 counts. For the water group ions we see the presence of several ghost peaks in the ST data; they occur at channels ~ 200 , 475 and about 1100. The peaks at 200-250 channel numbers are probably H^- ions coming out of the carbon foil of the IMS due to OH^+ , H_2O^+ , H_3O^+ and NH_3^+ incident ions which have hydrogen in them. The peak at 400 to 500 channel numbers are probably due to O^- ions coming out of the carbon foil of the IMS due to incident water group ions. The peak at channel numbers near 1100 are the LEF ghost peaks due to incident water group ions and ammonia ions. At Dione H^+ peaks at around 80 eV and occurs at ST channel 140 in TOF with its detectable LEF ghost peak at channel 260 (i.e., LEF ghost peak caused by H^+ ion striking LEF stop detector and secondary electron from LEF stop detector striking ST stop detector). Between 100 eV to 200 eV the ambient H_2^+ and pickup H_2^+ combine to form a single peak centered around ST channel 195; these ions would also be detectable using the LEF data. The water group ions at Dione are centered around channel 250 and 900 eV for the primary peak. O_2^+ peak occurs at around 1 keV and ST channel 850 for Dione, while the CO_2^+ peak is around 2 keV and ST channel 980 for Dione. In the case of Enceladus we see a similar result except that now the signal is confined below 1 keV, while for Dione counts extended up to 3 keV. This can be explained by the higher ambient co-rotation speeds and temperatures at Dione, and correspondingly larger pickup energies at Dione.

In the LEF data for Dione we see a clear peak for CO_2^+ at channel number 700 and $E/Q \sim 1$ -2 keV. At a slightly lower energy and LEF channel number of 950-1000 we see evidence of O_2^+ and

NH_3^+ . At around 500 eV we see clear evidence of O^+ and H_2O^+ ions between LEF channels 1000 and 1100. This data set will allow us to measure NH_3^+ . In the case of Enceladus the ion peaks are less pronounced, but we should be able to measure NH_3^+ , H_3O^+ , CO_2^+ and O_2^+ .

For a more quantitative determination we consider several cuts of the ST contour maps at specific E/Q . For Dione we consider $E/Q = 64$ eV, 724 eV and 1450 eV and are shown in Figure 16a. For Enceladus we consider $E/Q = 64$ eV, 362 eV, and 1024 eV and are displayed in Figure 17a. These cuts show the dominant presence of H^+ and H_2^+ below 100 eV, while at 724 eV for Dione and 362 eV for Enceladus the spectra are dominated by water group ions and finally at 1450 eV for Dione the dominant species are O_2^+ and CO_2^+ . For Enceladus O_2^+ is important at 1024 eV and CO_2^+ which is important at higher energies is barely seen at 1024 eV. At higher energies the peak at 200 to 250 ST channels is the H^- ghost peak due to water group ions, at ST channels 400 to 500 we are seeing O^- ghost peaks from the water group ions. Between ST channels 1100 to 1200 we see the LEF ghost peaks due to the water group ions. For each individual cut of the spectrogram we can apply the SAM (Spectrum Analyzer Module) algorithm (see Sittler, 1993) and de-convolve the mass peaks to obtain a more accurate estimate of ion counts for each species present in the data. The application of this algorithm is no more accurate than the accuracy of the calibration data. In order to acquire the ion counts for various ion species at specific E/Q from this data set we need to use the SAM algorithm. For this analysis we used a total of 10 ions which required us to invert a 10×10 coupling coefficient matrix to get a 10×10 inverse coupling coefficient matrix (Note, each individual cut contains the accumulated counts for 14 ions. For our de-convolution algorithm we only used 10 of those ions and correspondingly only included the accumulated counts for those 10 ions.). We then bin the data (i.e., sum the ion counts for a range of TOF channels centered on ion peak in TOF) for 10 ion species and multiply the binned

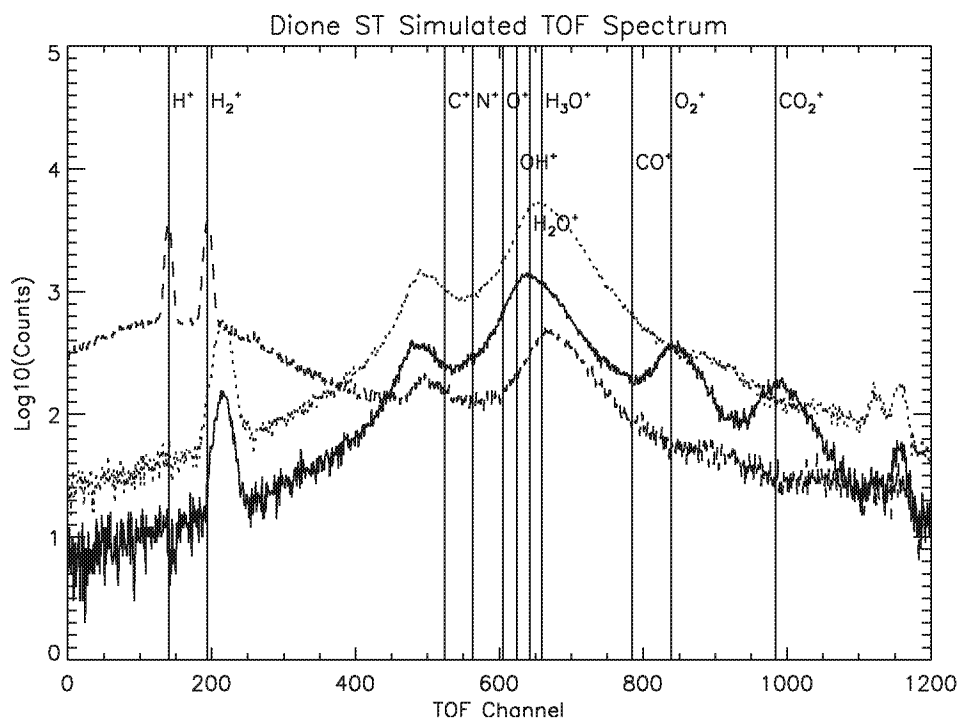


Figure 16a. Simulated ion counts versus TOF for B cycle ST data for Dione encounter. Each curve is a cut through the energy-TOF spectrogram at $E/Q = 64$ eV (—), 724 eV (···) and 1450 eV (——). Vertical lines give approximate peak positions for various incident ions.

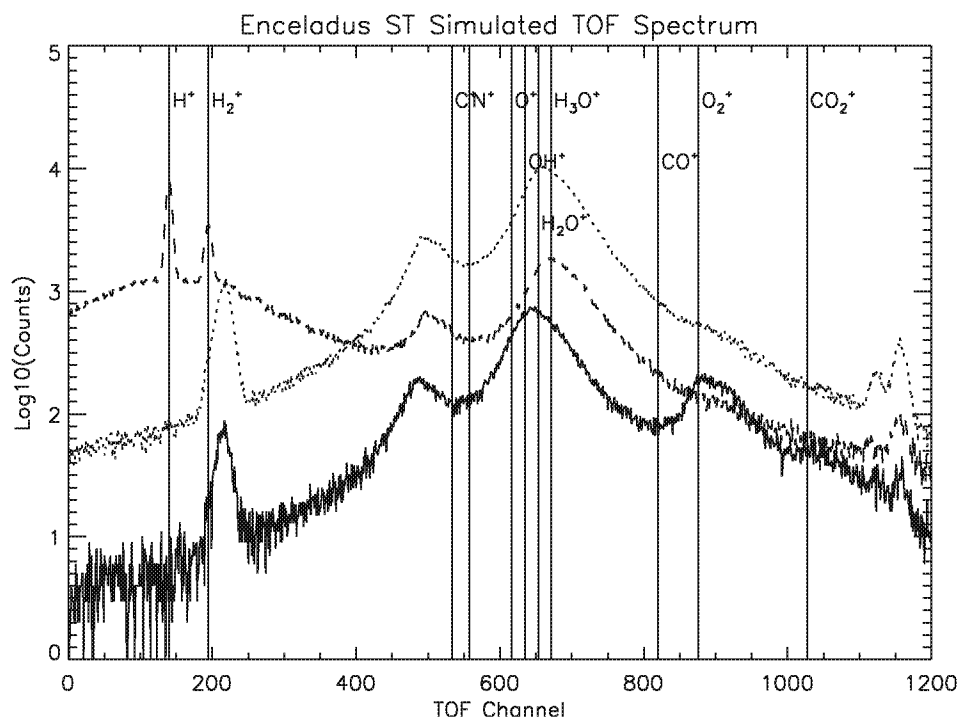


Figure 17a. Simulated ion counts versus TOF for B cycle ST data for Enceladus encounter. Each curve is a cut through the energy-TOF spectrogram at $E/Q = 64$ eV (—), 362 eV (···) and 1024 eV (——). Vertical lines give approximate peak positions for various incident ions.

data by the inverse coupling coefficient matrix to get the ion counts for each individual ion species. The details of applying this algorithm are described in Sittler (1993).

In Tables 5a and 5b we show for Dione and Enceladus, respectively, the de-convolved ion counts, $\langle C_{OUT} \rangle$, with error bars, σ_{COUT} , for the various ion species derived from a subset of the ST simulated spectra similar to that shown in Figures 16a and 17a. The $\langle C_{OUT} \rangle$ is an average computed from 40 solutions for which we added Poisson statistical noise to the simulated TOF spectra. The same can be said for our estimate of the standard deviation σ_{COUT} . The tables also show the input counts C_{IN} for ambient ions only and ambient ions plus pickup ions. We show the

ambient only counts to provide a baseline to determine our ability to separate the ambient ions from the pickup ions. In most cases, $\langle C_{OUT} \rangle \approx C_{IN}(\text{ambient+ring})$. The results show that one can separate the water group ions very well and shows the power of our de-convolution algorithm which we refer to as the SAM algorithm. For the water group ions the errors range from 1% to 6%. By comparing the ambient only and ambient plus pickup ion counts one can see that with the B cycle data it will be difficult to separate the pickup ions from the ambient ions for H^+ , H_2^+ , and O^+ . For the remaining ions OH^+ , H_2O^+ , H_3O^+ , O_2^+ , CO_2^+ and CO^+ we maybe able to separate them from the ambient ions when using the B cycle data when combined with the

Table 5a. Dione SAM ST Derived Ion Counts

Ion Type	E/Q (eV)	Resolution	C_{IN} (ambient)	C_{IN} (ambient+ring)	$\langle C_{OUT} \rangle$	σ_{COUT}
H^+	1450.0	ST	0.0	0.0	-1.65	8.82
“	724.0	“	0.0	0.0	-1.71	35.6
“	64.0	“	2.45E+5	2.61E+5	2.61E+5	637.0
H_2^+	1450.0	ST	0.0	0.0	-1.36	10.6
“	724.0	“	66.2	66.2	64.8	36.9
“	64.0	“	3.91E+4	4.87E+4	4.87E+4	317.0
O^+	1450.0	ST	2.12E+4	2.31E+4	2.33E+4	3771.0
“	724.0	“	7.88E+5	8.11E+5	8.11E+5	1.22E+4
“	64.0	“	4.48E+4	4.92E+4	4.88E+4	2809.0
$OH^+ + NH_3^+$	1450.0	ST	1.25E+4	2.44E+4	2.36E+4	8618.0
“	724.0	“	3.06E+5	3.66E+5	3.66E+5	2.66E+4
“	64.0	“	1.48E+4	2.86E+4	2.96E+4	6096.0
H_2O^+	1450.0	ST	1.47E+4	8.90E+4	8.99E+4	7728.0
“	724.0	“	2.51E+5	6.26E+5	6.26E+5	2.29E+4
“	64.0	“	1.05E+4	5.86E+4	5.76E+4	5154.0
H_3O^+	1450.0	ST	0.0	3.83E+3	3.16E+3	3.84E+3
“	724.0	“	0.0	1.85E+4	1.83E+4	1.11E+4
“	64.0	“	0.0	2357.0	2821.0	2522.0
O_2^+	1450.0	ST	6373.0	3.05E+4	3.05E+4	286.0
“	724.0	“	7445.0	2.17E+4	2.16E+4	270.0
“	64.0	“	120.0	2250.0	2247.0	89.0
CO_2^+	1450.0	ST	0.0	2.35E+4	2.35E+4	293.0
“	724.0	“	0.0	7811.0	7800.0	184.0
“	64.0	“	0.0	1991.0	1985.0	71.2
CO^+	1450.0	ST	0.0	681.0	699.0	160.0
“	724.0	“	0.0	482.0	482.0	224.0
“	64.0	“	0.0	73.0	52.4	79.6

Table 5b. Enceladus SAM ST Derived Ion Counts

Ion Type	E/Q (eV)	Resolution	C _{IN} (ambient)	C _{IN} (ambient+ring)	<C _{OUT} >	σ _{COUT}
H ⁺	1024	ST	0.0	0.0	-0.22	5.82
“	362	“	0.0	0.0	-6.45	41.7
“	64	“	2.12E+7	4.29E+5	4.29E+5	869.0
H ₂ ⁺	1024	ST	0.0	0.0	3.85	6.32
“	362	“	456.0	456.0	446.0	48.0
“	64	“	3.10E+4	3.15E+4	3.15E+4	279.0
O ⁺	1024	ST	4.49E+4	4.49E+4	4.51E+4	3228.0
“	362	“	2.01E+6	2.03E+6	2.03E+6	2.64E+4
“	64	“	3.64E+5	3.67E+5	3.65E+5	8019.0
OH ⁺ +NH ₃ ⁺	1024	ST	1.4E+4	1.40E+4	1.36E+4	7302.0
“	362	“	4.21E+5	4.51E+5	4.53E+5	5.56E+4
“	64	“	6.47E+4	7.39E+4	7.94E+4	1.76E+4
H ₂ O ⁺	1024	ST	2.53E+4	2.53E+4	2.53E+4	6364.0
“	362	“	6.24E+5	1.23E+6	1.23E+6	4.31E+4
“	64	“	9.56E+4	2.8E+5	2.75E+5	1.53E+4
H ₃ O ⁺	1024	ST	0.0	0.0	194.0	3065.0
“	362	“	0.0	2.03E+4	2.0E+4	1.91E+4
“	64	“	0.0	6069.0	8673.0	7535.0
O ₂ ⁺	1024	ST	0.0	1.57E+4	1.57E+4	177.0
“	362	“	0.0	2.3E+4	2.31E+4	256.0
“	64	“	0.0	5572.0	5539.0	122.0
CO ₂ ⁺	1024	ST	0.0	5565.0	5545.0	99.1
“	362	“	0.0	3290.0	3254.0	183.0
“	64	“	0.0	538.0	536.0	97.3
CO ⁺	1024	ST	0.0	18.5	-3.8	83.0
“	362	“	0.0	74.9	54.2	295.0
“	64	“	0.0	32.3	18.8	152.0

A cycle data. The primary reason for the ambiguity in the B cycle data is because we add the 8 angular sectors of the IMS together in the B cycle data. In the A cycle data we retain the energy-angle dependence of the ion counts. The advantage of the B cycle data is its greater sensitivity. Well determined ion counts for H⁺, H₂⁺, O₂⁺ and CO₂⁺ are estimated (i.e., errors ~

1%) because these species are well separated from each other and the water group ions. NH₃⁺ overlaps with OH⁺ and we are not able to distinguish between the two ions (i.e., one exception is the OH⁺ will produce an O⁻ ghost peak and NH₃⁺ will not). The detection of H₃O⁺ has a large uncertainty ~ 60% due to its co-location with the ambient ions O⁺, H₂O⁺ and OH⁺.

The LEF simulated B Cycle data, Figures 14b and 15b, shows singular peaks for atomic H^+ , H_2^+ , H_2O^+ and O^+ . The simulations also show shifted peak positions due to the presence of molecules; for example, the figure shows shifted peak for C^+ and O^+ for which the parent molecule is CO_2^+ ; CO^+ is present but is not resolved because of its low abundance relative to the other species. This shift results from the molecule breaking up in the carbon foil such that the exit speed from the carbon foil of the fragments is equal to the entrance speed of the parent molecule to the carbon foil. This causes a 15 keV CO^+ incident on carbon foil to have C^+ ion of energy 6.42 keV exiting carbon foil so that the fragment has sufficiently low enough energy that the detuning effect of the LEF section is important (see Nordholt et al., 1998). The energy dependence of LEF molecular peaks is that the peak position shifts to lower TOF with decreasing ion exit energy from the carbon foil. In order to calibrate our simulations we have taken as a standard, calibration data for N^+ and combined with the calibration data by Nordholt et al. (1998) to extend the coverage below 15 keV. For $E/Q > 15$ keV we fit the data with a power law in energy (i.e., $TOF = a \cdot E^c + b$ where a, b and c are determined from numerical fits to calibration data), while for $E/Q \leq 15$ keV we have fit the data with polynomial of order 3 (i.e., $TOF = ap + bp \cdot E + cp \cdot E^2 + dp \cdot E^3$ for which ap, bp, cp and dp are determined from numerical fits to calibration data). For the other ions we then multiply the above expression by $\sqrt{M/14}$ where M is the mass of the fragment exiting the carbon foil. In the case of $CO^+ \rightarrow C^+$ the mass $M = 12$ and energy $E = E_{co} + (12/28)$ which is then substituted into our polynomial expression for TOF. In reality more detailed calibration data will be required under real conditions. These results are accurate enough to display the effects expected based on instrument response.

Using the data from Nordholt et al. (1998) Figure 6 we have also estimated the probability for a C^+ fragment ($P = 0.79$) relative to that for an O^+ fragment ($P = 0.21$) for which the parent

molecule is CO^+ . A similar calculation can be done for CO_2^+ for which $P = 0.65$ for C^+ and $P = 0.35$ for O^+ . Inspection of Figure 14b shows no evidence of CO^+ at $TOF \sim 780$ which means that the peak at about $TOF \sim 980$ is due to NH_3^+ . One can see from these same figures the shift of H_2^+ from H^+ to lower TOF so that it is well separated from the H^+ peak. We also see a well separated peak for NH_3^+ from N^+ and H_2O^+ from O^+ . We also see a well resolved peak for $O_2^+ \rightarrow O^+$; because of this we can uniquely separate O_2^+ from S^+ . While for the ST simulations this separation of peaks is not always possible. The simulations also underscore the importance of having good calibration data. In some instances the ST data can better separate the ions of different M/Q , while the LEF data is best for separating atomic and molecular species of similar M/Q . It should also be emphasized that in many cases the LEF feature of the IMS will provide a unique separation of molecules from molecules and atomic ions of the same M/Q . For example, the Nordholt et al. (1998) results in Figure 6 of that paper show how the $CO^+ \rightarrow C^+$ and $CO^+ \rightarrow O^+$ peaks are well separated from the $N_2^+ \rightarrow N^+$ peak; for which CO^+ and N_2^+ have the same M/Q . Also, ^{40}Ar will be well separated from CO_2^+ which has $M/Q=44$. It should be clear from these results that CAPS should be able to separate the molecules from the corresponding atomic species. Again, the main difference between Figure 14b and Figure 15b is that for Enceladus the ion peaks are confined to lower energy relative to that for Dione. Because the ions are measured at lower energy for Enceladus, the LEF TOF peaks will be shifted to lower TOF for Enceladus relative to that for Dione. In the case of the ST data the inverse is true. Here, we emphasize the fact that the water group ions are not well resolved in the ST data while for the LEF data they are resolved to a greater extent.

In Figures 16b and 17b we show cuts through the LEF E/Q versus TOF spectrograms for Dione and Enceladus, respectively, with $E/Q = 64$ eV, 724 eV and 1450 eV for Dione and $E/Q = 64$ eV, 362 eV and 1024 eV for Enceladus. For

Dione we see at $E/Q < 100$ eV well resolved peaks for H^+ , H_2^+ , $NH_3^+ \rightarrow N^+$, $H_2O^+ \rightarrow O^+$ and O^+ . At $E/Q = 724$ eV for Dione we see well resolved peaks for $CO_2^+ \rightarrow C^+$, $CO_2^+ \rightarrow O^+$, $O_2^+ \rightarrow O^+$, $NH_3^+ \rightarrow N^+$, $H_2O^+ \rightarrow O^+$ and O^+ . These spectra show the power of the LEF feature of the IMS in that the species NH_3^+ , N^+ , H_2O^+ and O^+ can be separated, while for ST data it would not be possible to do very accurately. At $E/Q = 1450$ eV for Dione the spectrum is dominated by peaks for $CO_2^+ \rightarrow C^+$, $CO_2^+ \rightarrow O^+$, $O_2^+ \rightarrow O^+$, $NH_3^+ \rightarrow N^+$, $H_2O^+ \rightarrow O^+$ and O^+ . The cuts in E/Q for Enceladus show peaks for H^+ , H_2^+ at 64 eV and peaks for $O_2^+ \rightarrow O^+$, $NH_3^+ \rightarrow N^+$, $H_2O^+ \rightarrow O^+$ and O^+ . At 362 eV at Enceladus we have the same result except the H^+ , H_2^+ ions are missing, the $CO_2^+ \rightarrow C^+$ peak appears and the NH_3^+ peak is still well resolved from the $O_2^+ \rightarrow O^+$ peak. Finally, at 1024 eV for Enceladus we only see peaks due to $CO_2^+ \rightarrow C^+$, $O_2^+ \rightarrow O^+$, $H_2O^+ \rightarrow O^+$ and O^+ . For Enceladus we do not see any obvious evidence of N^+ in the simulated data.

Similar to what we did for the ST data we are now in a position to apply the SAM algorithm (Sittler, 1993) to our cuts through the LEF spectrograms. In Tables 5b and 5d we show for Dione and Enceladus, respectively, the de-convolved ion counts with error bars for the various ion species derived from the LEF simulated spectra shown in Figures 16b and 17b. The results show that one can separate the water group ions fairly well (i.e., uncertainties $\sim 1\%$) with only the H_3O^+ having relatively large uncertainties $\sim 15\%$. Well determined ion counts for H^+ , H_2^+ , O_2^+ and CO_2^+ are estimated because these species are well separated from each other and the water group ions (i.e., errors $\sim 2\%-3\%$). For the LEF data we were able to include NH_3^+ in our solutions whose peak is well resolved from the water group ions; estimated errors are $\sim 3\%-4\%$. The data also show that we should be able to resolve the pickup ions from the ambient ions using the A cycle and B cycle data for ions H_2^+ , NH_3^+ , OH^+ , H_2O^+ , H_3O^+ , O_2^+ , CO_2^+ and CO^+ .

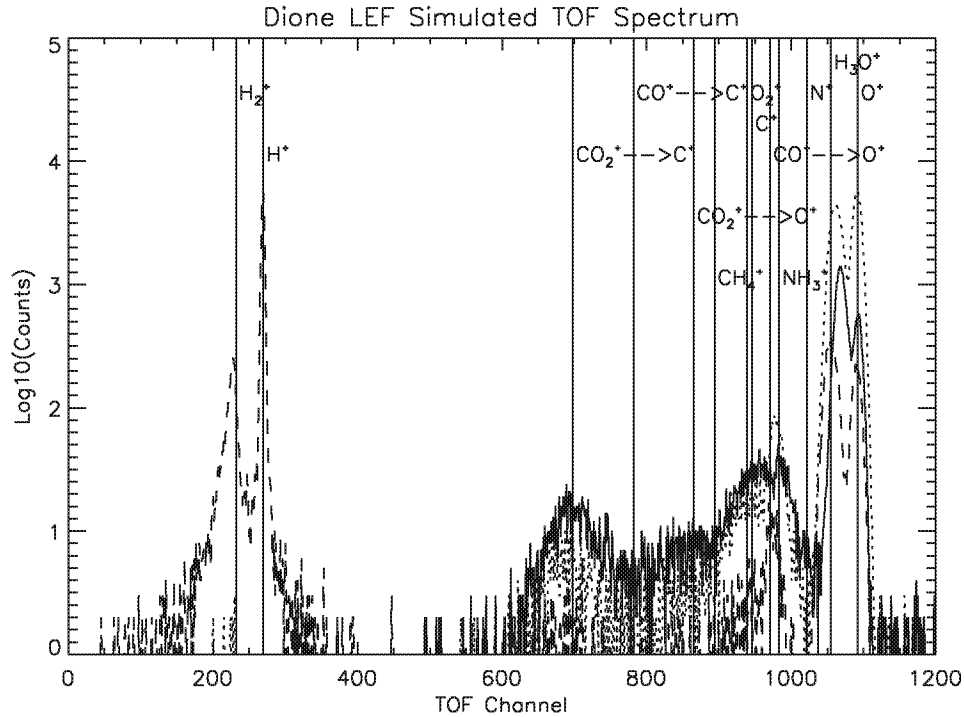


Figure 16b. Simulated ion counts versus TOF for B cycle LEF data for Dione encounter. Each curve is a cut through the energy-TOF spectrogram at $E/Q = 64$ eV (—), 724 eV (···) and 1450 eV (---). Vertical lines give approximate peak positions for various incident ions.

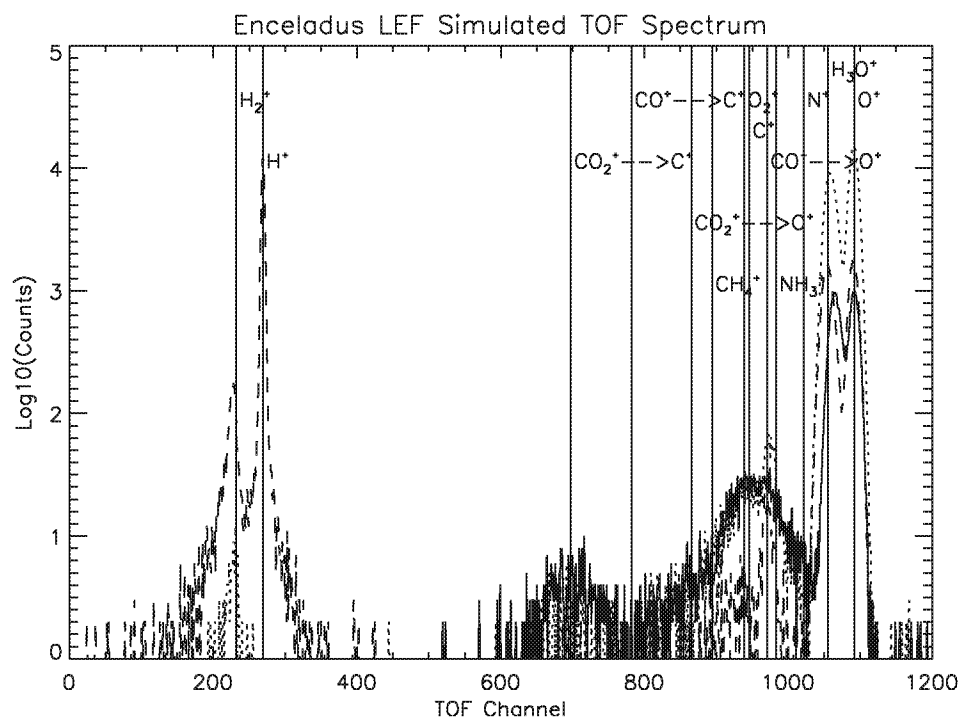


Figure 17b. Simulated ion counts versus TOF for B cycle LEF data for Enceladus encounter. Each curve is a cut through the energy-TOF spectrogram at $E/Q = 64$ eV (—), 362 eV (···) and 1024 eV (---). Vertical lines give approximate peak positions for various incident ions.

Table 5c. Dione SAM LEF Derived Ion Counts

Ion Type	E/Q (eV)	Resolution	C _{IN} (ambient)	C _{IN} (ambient+ring)	<C _{OUT} >	σ _{COUT}
H ⁺	1450.0	LEF	0.0	0.0	0.1	0.74
“	724.0	“	0.0	0.0	0.03	0.48
“	64.0	“	2.45E+4	2.61E+4	2.6E+4	172.0
H ₂ ⁺	1450.0	LEF	0.0	0.0	0.23	1.2
“	724.0	“	6.62	6.62	6.14	2.78
“	64.0	“	3907.0	4872.0	4887.0	104.0
NH ₃ ⁺	1450.0	LEF	0.0	271.0	266.0	20.7
“	724.0	“	0.0	1360.0	1355.0	49.7
“	64.0	“	0.0	313.0	306.0	19.3
O ⁺	1450.0	LEF	2118.0	2309.0	2320.0	67.3
“	724.0	“	7.88E+4	8.11E+4	8.11E+4	313.0
“	64.0	“	4475.0	4923.0	4914.0	76.7
OH ⁺	1450.0	LEF	1246.0	2168.0	2148.0	171.0
“	724.0	“	3.06E+4	3.52E+4	3.51E+4	422.0
“	64.0	“	1476.0	2542.0	2578.0	117.0
H ₂ O ⁺	1450.0	LEF	1470.0	8899.0	8878.0	205.0
“	724.0	“	2.51E+4	6.26E+4	6.27E+4	526.0
“	64.0	“	1054.0	5859.0	5819.0	160.0
H ₃ O ⁺	1450.0	LEF	0.0	368.0	379.0	100.0
“	724.0	“	0.0	1851.0	1873.0	292.0
“	64.0	“	0.0	236.0	250.0	67.3
O ₂ ⁺	1450.0	LEF	637.0	3049.0	3039.0	69.4
“	724.0	“	745.0	2168.0	2163.0	52.6
“	64.0	“	12.0	225.0	223.0	22.2
CO ₂ ⁺	1450.0	LEF	0.0	2350.0	2337.0	73.9
“	724.0	“	0.0	781.0	786.0	48.1
“	64.0	“	0.0	199.0	199.0	27.0
CO ⁺	1450.0	LEF	0.0	68.0	70.4	30.4
“	724.0	“	0.0	48.2	46.4	19.5
“	64.0	“	0.0	7.3	7.84	10.0

Table 5d. Enceladus SAM LEF Derived Ion Counts

Ion Type	E/Q (eV)	Resolution	C _{IN} (ambient)	C _{IN} (ambient+ring)	<C _{OUT} >	σ _{COUT}
H ⁺	1024	LEF	0.0	0.0	0.0	0.3
“	362	“	0.0	0.0	0.24	0.72
“	64	“	2.12E+6	4.29E+4	4.29E+4	228.0
H ₂ ⁺	1024	LEF	0.0	0.0	0.0	0.44
“	362	“	45.6	45.6	47.2	9.3
“	64	“	3096.0	3150.0	3155.0	70.8
NH ₃ ⁺	1024	LEF	0.0	0.0	4.58	11.4
“	362	“	0.0	879.0	879.0	36.8
“	64	“	0.0	265.0	262.0	24.7
O ⁺	1024	LEF	4486.0	4486.0	4470.0	96.1
“	362	“	2.01E+5	2.03E+5	2.03E+5	530.0
“	64	“	3.64E+4	3.67E+4	3.67E+4	233.0
OH ⁺	1024	LEF	1402.0	1402.0	1387.0	114.0
“	362	“	4.21E+4	4.42E+4	4.41E+4	627.0
“	64	“	6471.0	7125.0	7108.0	242.0
H ₂ O ⁺	1024	LEF	3095.0	3095.0	3102.0	145.0
“	362	“	6.5E+4	1.25E+5	1.25E+5	763.0
“	64	“	8679.0	2.67E+4	2.67E+4	325.0
H ₃ O ⁺	1024	LEF	0.0	0.0	-6.21	68.2
“	362	“	0.0	2031.0	1919.0	470.0
“	64	“	0.0	607.0	594.0	181.0
O ₂ ⁺	1024	LEF	353.0	1570.0	1566.0	43.1
“	362	“	538.0	2304.0	2311.0	61.7
“	64	“	26.7	557.0	557.0	24.9
CO ₂ ⁺	1024	LEF	0.0	556.0	555.0	36.5
“	362	“	0.0	329.0	342.0	26.0
“	64	“	0.0	53.8	55.2	11.4
CO ⁺	1024	LEF	0.0	1.85	5.2	12.4
“	362	“	0.0	7.5	5.25	13.6
“	64	“	0.0	3.23	3.96	6.67

7. Summary and Conclusion

We have presented a model of the sputtered atmospheres for Dione and Enceladus where for simplicity we assumed spherical symmetry. We have used the maximum source rate estimated by Jurac et al. (2001) for both these bodies. Here the dominant sputtered species is H_2O with a 10% contribution from O_2 , H_2 , CO_2 and NH_3 . In the case of Dione and Enceladus the maximum neutral density at the surface is a few times 10^5 mol/cm³ for H_2O with the neutral density varying roughly like $1/r^3$ with distance from the satellite near the body and $1/r^2$ far from the body. A measurement of the radial variation of the neutral density can provide information about the energy spectrum of the sputtered neutrals (i.e., determine parameter U). By measuring the height dependence of the pickup ion densities one can reconstruct the height dependence of the neutrals. We also speculated about the possibility of a gravitationally bound atmosphere of O_3 and O_2 because of the detection of ozone at Dione (Noll et al., 1997). This atmosphere, if present, would be considerably denser than that estimated for a sputtered atmosphere and pickup ion densities could be dominated by O_2^+ and O_3^+ . One could readily detect the presence of Argon 40 as radioactive decay product which would also be gravitationally bound to Dione and Enceladus, respectively.

We computed the pickup ion densities as a function of height by assuming a weak interaction between the magnetosphere of Saturn and the icy satellites atmosphere. We also assumed a fluid approximation and neglected finite gyro-radius effects which was substantiated by the smallness of the ion gyro-radius for pickup water ions with respect to the satellite radius. In both cases water ions dominated the pickup ion density reaching peak values of 1.0 mol/cm³ and 2.2 mol/cm³ for Dione and Enceladus, respectively. For a wake pass at the surface of Dione in order of most abundant we have O_2^+ , OH^+ , CO_2^+ , H^+ , H_3O^+ , NH_3^+ , O^+ , H_2^+ and NH_2^+ . In the case of Enceladus we have in the order of most abundant at the surface O_2^+ , H_3O^+ , OH^+ , NH_3^+ and

CO_2^+ . At much lower abundance we have NH_2^+ , H^+ , O^+ and H_2^+ .

We used the pickup ion densities at the surface to compute the ring distributions that would result and plotted them as a function of E/Q and angle in Saturn's equatorial plane. These simulations showed the high degree of detection for the pickup ions, even when the densities were low. This is because the pickup ions obey a delta function velocity distribution which translates into a high concentration of the ions in phase space. The flux peaks at twice the pickup velocity. We used these results to show the energy-angle coverage provided by CAPS gives us ability to resolve the pickup ion distributions from the ambient plasma ions. The energy-pitch angle dependence of the pickup ions is considerably different from that of the ambient ions which obey convected Maxwellians.

We also computed simulated energy-TOF spectrograms for the Dione flyby and the Enceladus flyby. This data is referred to as B cycle data (see Young et al. (2000)) and is accumulated over several thousand kilometers and thus provide no spatial resolution of the encounter. The simulations showed that the ST data could be used to separate most of the ions observed by CAPS but with considerable uncertainty for some of the minor water group ions, N^+ and NH_3^+ . The other ions H^+ , H_2^+ , O_2^+ and CO_2^+ were well resolved by the CAPS ST data. While, the LEF data allowed us to resolve the water group ions, N^+ and NH_3^+ . In the case of CO_2^+ the LEF data was preferred since it gave a unique identification of CO_2^+ . The same can be said for O_2^+ and uniquely separating from S^+ . The LEF data also provides the potential for uniquely detecting CO^+ or N_2^+ . Therefore, when we detect different ion species for high spatial, energy and angle resolution we will use a combination of ST and LEF data to make the ion identification. This will be done by binning the ions over specified intervals of TOF and then applying the SAM algorithm. For the B cycle data we will be able to analyze the energy-TOF spectrograms with the maximum resolution

in TOF and species and to detect very minor pickup species such as H_2^+ .

In conclusion, CAPS provides a unique capability in determining the composition of the surfaces of the icy satellites of Saturn (see Johnson and Sittler, 1990). Our simulations have shown CAPS ability to detect the various ion species well above background in most cases, and thus infer the bulk composition of the icy satellites. Our simulations have not included background effects, but is not expected to be important in most cases; at most it will just raise the uncertainty in our determinations. The background could be as high as 1% the peak count rate of the dominant species at the energy the dominant species is measured. The background will tend to be flat in TOF with an increase toward smaller TOF. These corrections, which are also a function of the penetrating radiation flux, will be included under real measurement conditions. For example, if the dominant ion has a peak count of 10^5 and the background is 1% or 10^3 counts, then the uncertainty due to background will be ~ 30 counts. (Here we note that this background is primarily caused by the scattering of ions as they pass through the carbon foil of the spectrometer and their accidental detection by the start detectors.) With regard to background corrections they will be more severe for Enceladus than Dione because the radiation belt intensities are greater at Enceladus; the back-

ground is made worse by penetrating radiation as demonstrated by the Cassini Earth flyby data. Then the background could be more than a few percent. At present we are analyzing the background corrections due to penetrating radiation using the Earth flyby data. We also emphasize, because of background corrections, that if we want to detect minor ions which could be around the few % level relative to O^+ such as NH_3^+ will be very difficult to detect for an upstream pass while possible for a wake pass. In the case of NH_3^+ we must use LEF data which has a sensitivity a factor of 10 less than ST data. We have also argued that the closer the spacecraft encounters the moon the better, in order to minimize the diluting effect of scattering which will make the ion detection more difficult. A rough calculation indicates that pitch angle scattering of 5° will dilute the pickup ions by a factor of 2; here the pickup ions are confined centrifugally. We do plan to dither the entrance collimator above and below Saturn's equatorial plane to look for scattering effects. Finally, our calculations with regard to the interaction are not self-consistent since we have assumed a weak interaction; here we note the possibility for a strong strength interaction at Dione, for which we note the detection of ion cyclotron waves centered on the L shell of Dione by Pioneer 11 and Voyager 1. These waves are consistent with pickup ions such as the water group ions.

References

1. Baragiola, R. A., R. Vidal, M. Shi, W. Svendsen, J. Schou and D. Bahr, Sputtering of ices, submitted to Scanning Microscopy, 1999.
2. Barbosa, D.D., Theory and observations of electromagnetic ion cyclotron waves in Saturn's inner magnetosphere, *J. Geophys. Res.*, **98**, 9345, 1993.
3. Bar-Nun, A., G. Herman, and Yu Melker, Ejection of H₂O, O₂, H₂ and H from water ice by 0.5-6 keV H⁺ and Ne⁺ ion bombardment, *Surface science*, **150**, 143, 1985.
4. Brown, R., et al., Visible Infrared Mapping Spectrometer (VIMS) on Cassini, *Space Science Reviews*, submitted, 2002.
5. Fillius, W. and C. E. McIlwain, Trapped radiation belts of Saturn: First Look, *Science*, **207**, 425, 1980a.
6. Fillius, W. and C. E. McIlwain, Very energetic protons in Saturn's radiation belt, *J. Geophys. Res.*, **85**, 5803, 1980b.
7. Frank, L. A., B. G. Burek, K. L. Ackerson, J. H. Wolfe and J. D. Mihalov, Plasmas in Saturn's magnetosphere, *J. Geophys. Res.*, **85**, 5695, 1980.
8. Gurnett, D., et al., Radio and Plasma Wave Science Investigation for Cassini, *Space Science Reviews*, submitted, C. T. Russell Editor, 2002.
9. Hall, D. T., P. D. Feldman, J. B. Holberg, M. A. McGrath, Florescent hydroxyl emissions from Saturn's ring atmosphere, *Science*, **272**, 516, 1996.
10. Hamilton, D. P. and J. A. Burns, Origin of Saturn's E ring: Self sustained, naturally, *Science*, **264**, 550, 1994.
11. Hanel, R. A., B. J. Conrath, F. M. Flasar, V. G. Kunde, W. Maguire, J. C. Pearl, J. A. Pirraglia, R. Samuelson, L. Hearsh, M. Allison, D. P. Cruikshank, D. Gautier, P. Gierrasch, L. Horn, R. Koppany and C. Ponnampuruma, Infrared observations of the Saturnian system from Voyager 2, *Science*, **212**, 192, 1981.
12. Hanel, R. A., B. J. Conrath, F. M. Flasar, V. G. Kunde, W. Maguire, J. C. Pearl, J. A. Pirraglia, R. Samuelson, D. P. Cruikshank, D. Gautier, P. Gierrasch, L. Horn, R. Koppany and C. Ponnampuruma, Infrared observations of the Saturnian system from Voyager 2, *Science*, **215**, 544, 1982.
13. Ip, W. H., On neutral cloud distributions in the Saturnian magnetosphere, *Icarus*, **126**, 42, 1997.
14. Johnson, R. E., M. K. Pospieszalska, E. C. Sittler Jr., A. F. Cheng, L. J. Lanzerotti, and E. M. Sievka, The neutral cloud and heavy ion inner torus at Saturn, *Icarus*, **77**, 311, 1989.
15. Johnson, R. E., Energetic charged-particle interactions with atmospheres and surfaces, Springer-Verlag, Berlin, 1990.
16. Johnson, R. E., Sputtering and desorption from icy surfaces. In: B. Schmitt, C. deBergh (Eds.), *Solar System Ices*, Kluwer, Netherlands, 303, 1998.
17. Johnson, R. E. and E. C. Sittler Jr., Sputter-produced plasma as a measure of satellite surface composition: The Cassini mission, *Geophys. Res. Lett.*, **17**, 1629, 1990.
18. Jurac, S., R. E. Johnson, J. D. Richardson and C. Paranicas, Satellite sputtering in Saturn's magnetosphere, *Planetary and Space Science*, **49**, 319, 2001..

19. Kivelson, M. G., J. Warnecke, L. Joy S. Bennett, K. K. Khurana, J. A. Linker, C. T. Russell, R. J. Walker, and C. Polanskey, Ganymede's magnetosphere: Magnetometer overview, *J. Geophys. Res.-Planets*, **103**, 19963, 1998.
20. Kivelson, M. G., K. K. Khurana, C. T. Russell, M. Volwerk, R. J. Walker and C. Zimmer, *Science*, **289**, 1340, 2000.
21. Krimigis, S. M. and T. P. Armstrong, Two-component proton spectra in the inner Saturnian magnetosphere, *Geophys. Res. Lett.*, **9**, 1143, 1982.
22. Krimigis, S. M., J. F. Carbary, E. P. Keath, T. P. Armstrong, L. J. Lanzerotti, and G. Gloeckler, General characteristics of hot plasma and energetic particles in the Saturnian magnetosphere: Results from the Voyager spacecraft, *J. Geophys. Res.*, **88**, 8871, 1983.
23. Krimigis et al., Magnetospheric Imaging Instrument on Cassini, *Space Science Reviews*, submitted, 2002.
24. Kunde, V. G., et al., The Composition Infrared Spectrometer (CIRS) Experiment on Cassini, *Exploring the Saturn System in the Thermal Infrared*, manuscript in preparation, C. T. Russell Editor, 2002.
25. Lazarus, A. J. and R. L. McNutt Jr., Low energy plasma ion observations in Saturn's magnetosphere, *J. Geophys. Res.*, **88**, 8831, 1983.
26. Lutz, B. L., C. de Bergh and T. Owen, Titan: Discovery of carbon monoxide in its atmosphere, *Science*, **220**, 1374, 1983.
27. Ma, T.Z., D.A. gurnett and C.K. Goertz, Interpretation of electrostatic noise observed by Voyager 1 in Titan's wake, *J. Geophys. Res.*, **92**, 8595, 1987.
28. Maurice, S., E. C. Sittler Jr., J. F. Cooper, B. H. Mauk, M. Blanc, and R. S. Selesnick, Comprehensive analysis of electron observations at Saturn: Voyager 1 and 2, *J. Geophys. Res.*, **101**, 15211, 1996.
29. McCord, T. B. et al., Organics and other molecules in the surfaces of Ganymede and Callisto, *Science*, **280**, 1242, 1998.
30. Morrison, D., T. V. Johnson, E. M. Shoemaker, L. A. Soderblom, P. Thomas, J. Veverka and B. A. Smith, Satellites of Saturn: Geological Perspective, *Saturn*, edited by T. Gehrels and M. S. Matthews, The University of Arizona Press, 1984.
31. Neubauer, F.M., D.A. Gurnett, J.D. Scudder, and R.E. Hartle, Titan's magnetospheric interaction, *Saturn*, edited by T. Gehrels and M. S. Matthews, University of Arizona Press, 760, 1984.
32. Noll, K. S., T. Rousch, D. Cruikshank and R. E. Johnson, Detection of ozone on Saturn's satellites Dione and Rhea, *Nature*, **388**, 45, 1997.
33. Paranicas, C., A. F. Cheng, B. H. Mauk, E. F. Keath, S. M. Krimigis, Evidence of a source of energetic ions at Saturn, *J. Geophys. Res.*, **104**, 17459, 1997.
34. Richardson, J. D., Thermal ions at Saturn: Plasma parameters and implications, *J. Geophys. Res.*, **91**, 1381, 1986.
35. Richardson, J. D., A. Eviatar and G. L. Siscoe, Satellite Tori at Saturn, *J. Geophys. Res.*, **91**, 8749, 1986.
36. Richardson, J. D., A. Eviatar, M. A. McGrath, and V. M. Vasyliunas, OH in Saturn's magnetosphere: Observations and implications, *J. Geophys. Res.*, **103**, 20245, 1998.

37. Richardson, J. D. and E. C. Sittler Jr., A plasma density model for Saturn based on Voyager observations, *J. Geophys. Res.*, **95**, 12019, 1990.
38. Russell, C. T. and D. E. Huddleston, Ion-cyclotron waves at Io, *Planetary ionospheres and magnetospheres*, **26**, 1505, 2000.
39. Russell, C. T., D. E. Huddleston, K. K. Khurana and M. G. Kivelson, *Planetary ionospheres and magnetospheres*, **26**, 1489, 2000.
40. Samuelson, R. E., W. C. Maguire, R. A. Hanel, V. G. Kunde, D. E. Jennings, Y. L. Yung, and A. C. Aikin, CO₂ on Titan, *J. Geophys. Res.*, **88**, 8709, 1983.
41. Schardt, A. W. and F. B. McDonald, The flux and source of energetic protons in Saturn's inner magnetosphere, *J. Geophys. Res.*, **88**, 8923, 1983.
42. Shemansky, D. E., P. Matherson, D. T. Hall, H. Y. Hu and T. M. Tripp, Detection of the hydroxyl radical in the Saturn magnetosphere, *Nature*, **363**, 329, 1993.
43. Shi, M., R. A. Baragiola, D. E. Grosjean, R. E. Johnson, S. Jurac and J. Schou, Sputtering of water ice surfaces and the production of extended neutral atmospheres, *J. Geophys. Res.*, **100**, 26387, 1995.
44. Sittler, E. C., Jr., K. W. Ogilvie and J. D. Scudder, Survey of low energy plasma electrons in Saturn's magnetosphere: Voyager 1 and 2, *J. Geophys. Res.*, **88**, 8847, 1983.
45. Sittler, E. C., Jr., Real-time spectral analysis algorithm for space plasma three-dimension ion mass spectrometers, *Rev. Sci. Instr.*, **64**, 2771, 1993.
46. Smith, E. J. and B. T. Tsurutani, Saturn's magnetosphere: Observations of ion cyclotron waves near the Dione L shell, *J. Geophys. Res.*, **88**, 7831, 1983.
47. Stevenson, D. J., Volcanism and igneous processes in small icy satellites, *Nature*, **298**, 142, 1982.
48. Van Allen, J. A., Energetic particles in the inner magnetosphere of Saturn, *Saturn*, edited by T. Gehrels and M. S. Matthews, The University of Arizona Press, 1984.
49. Vasyliunas, V. M. and G. L. Siscoe, On the flux and the energy spectrum of interstellar ions in the solar system, *J. Geophys. Res.*, **81**, 1247, 1976.
50. Vogt, R. E., D. L. Chenette, A. C. Cummings, T. L. Garrard, E. C. Stone, A. W. Schardt, J. H. Trainor, N. Lal, and F. B. McDonald, Energetic charged particles in Saturn's magnetosphere: Voyager 1 results, *Science*, **212**, 231, 1981.
51. Vogt, R. E., D. L. Chenette, A. C. Cummings, T. L. Garrard, E. C. Stone, A. W. Schardt, J. H. Trainor, N. Lal, and F. B. McDonald, Energetic charged particles in Saturn's magnetosphere: Voyager 2 results, *Science*, **215**, 577, 1982.
52. Young, D. T., et al., Cassini Plasma Spectrometer Investigation, *Space Science Reviews*, submitted, C. T. Russell Editor, 2002.
53. Zimmer, C., K. K. Khurana and M. G. Kivelson, Subsurface oceans on Europa and Callisto: Constraints from Galileo magnetometer observations, *Icarus*, **147**, 329, 2000.

REPORT DOCUMENTATION PAGE			Form Approved OMB No. 0704-0188	
Public reporting burden for this collection of information is estimated to average 1 hour per response, including the time for reviewing instructions, searching existing data sources, gathering and maintaining the data needed, and completing and reviewing the collection of information. Send comments regarding this burden estimate or any other aspect of this collection of information, including suggestions for reducing this burden, to Washington Headquarters Services, Directorate for Information Operations and Reports, 1215 Jefferson Davis Highway, Suite 1204, Arlington, VA 22202-4302, and to the Office of Management and Budget, Paperwork Reduction Project (0704-0188), Washington, DC 20503.				
1. AGENCY USE ONLY (Leave blank)		2. REPORT DATE August 2002		3. REPORT TYPE AND DATES COVERED Technical Memorandum
4. TITLE AND SUBTITLE Pickup Ions at Dione and Enceladus			5. FUNDING NUMBERS Code 692	
6. AUTHOR(S) E. Sittler, R.E. Johnson, S. Jurac, J. Richardson, M. McGrath, F. Crary, D. Young, and J.E. Nordholt				
7. PERFORMING ORGANIZATION NAME(S) AND ADDRESS (ES) Goddard Space Flight Center Greenbelt, Maryland 20771			8. PERFORMING ORGANIZATION REPORT NUMBER 2002-03030-0	
9. SPONSORING / MONITORING AGENCY NAME(S) AND ADDRESS (ES) National Aeronautics and Space Administration Washington, DC 20546-0001			10. SPONSORING / MONITORING AGENCY REPORT NUMBER TM-2002-211612	
11. SUPPLEMENTARY NOTES R.E. Johnson, University of Virginia, Charlottesville, VA; S. Jurac, J. Richardson, Massachusetts Institute of Technology, Cambridge, MA; M. McGrath, Space Telescope Institute, Baltimore, MD; F. Crary, D. Young, University of Michigan, Ann Arbor, MI; J.E. Nordholt, Los Alamos National Laboratory, NM				
12a. DISTRIBUTION / AVAILABILITY STATEMENT Unclassified-Unlimited Subject Category: 91 Report available from the NASA Center for AeroSpace Information, 7121 Standard Drive, Hanover, MD 21076-1320. (301) 621-0390.			12b. DISTRIBUTION CODE	
13. ABSTRACT (Maximum 200 words) Voyager images of the icy satellites of Saturn, Dione and Enceladus, suggest they have been geologically active and are not only composed of ice. Recent observations by HST have shown the presence of ozone at both Dione and Rhea which also implies the presence of molecular oxygen at these bodies. The Cassini Plasma Spectrometer (CAPS) will provide the capability to determine the global composition of these bodies by measuring the pickup ions produced by the ionization of their sputter produced atmospheres. We will present a model of these atmospheres and associated pickup ions and demonstrate CAPS ability to distinguish the freshly produced picked up ions from the ambient plasma. Such ions are expected to form a ring distribution that will have a uniquely different energy-angle dependence than the ambient plasma ions. In the case of Dione we expect the potential for a moderate strength interaction for which both Voyager 1 and Pioneer 11 spacecraft measured ion cyclotron waves centered on the Dione L shell and near the equatorial plane. Since Enceladus may be the source of the E-ring, some surprises may be encountered during its close encounter with the Cassini spacecraft. In the case of Dione we will show that a wake pass at 500 km altitude is more than an order of magnitude better than an upstream pass at 500 km altitude. Pickup ion detection for minor ion species such as NH_3^+ is possible for 500 km altitude wake pass but not for a 500 km altitude upstream pass at closest approach. For navigation reasons a 100 km pass is not allowed and therefore it is essential to have a wake pass to maximize the science return for a targeted flyby with Dione. The CAPS observations when combined with magnetometer, plasma wave and energetic particle observations will allow us to estimate the source of ions into Saturn's magnetosphere due to these two bodies and to characterize the nature of the interaction with Saturn's magnetosphere.				
14. SUBJECT TERMS Dione, Enceladus, Cassini Plasma Spectrometer (CAPS), Cassini, Saturn			15. NUMBER OF PAGES 42	
			16. PRICE CODE	
17. SECURITY CLASSIFICATION OF REPORT Unclassified	18. SECURITY CLASSIFICATION OF THIS PAGE Unclassified	19. SECURITY CLASSIFICATION OF ABSTRACT Unclassified	20. LIMITATION OF ABSTRACT UL	

